Review

Bei-Bei Li*, Lingfeng Ou, Yuechen Lei and Yong-Chun Liu*

Cavity optomechanical sensing

https://doi.org/10.1515/nanoph-2021-0256
Received May 23, 2021; accepted July 4, 2021;
published online August 24, 2021

Abstract: Cavity optomechanical systems enable interactions between light and mechanical resonators, providing a platform both for fundamental physics of macroscopic quantum systems and for practical applications of precision sensing. The resonant enhancement of both mechanical and optical response in the cavity optomechanical systems has enabled precision sensing of multiple physical quantities, including displacements, masses, forces, accelerations, magnetic fields, and ultrasounds. In this article, we review the progress of precision sensing applications using cavity optomechanical systems. The review is organized in the following way: first we will introduce the physical principles of optomechanical sensing, including a discussion of the noises and sensitivity of the systems, and then review the progress in displacement sensing, mass sensing, force sensing, atomic force microscope (AFM) and magnetic resonance force microscope (MRFM), accelerometry, magnetometry, and ultrasound sensing, and introduce the progress of using quantum techniques especially squeezed light to enhance the performance of the optomechanical sensors. Finally, we give a summary and outlook.

Keywords: cavity optomechanics; microresonators; on-chip photonic devices; precision sensing; squeezed light.

***Corresponding authors: Bei-Bei Li**, Beijing National Laboratory for Condensed Matter Physics, Institute of Physics, Chinese Academy of Sciences, Beijing 100094, P. R. China; and Songshan Lake Materials Laboratory, Dongguan 523808, Guangdong, P. R. China, E-mail: libeibei@iphy.ac.cn. https://orcid.org/0000-0002-9259-244X; and **Yong-Chun Liu**, Department of Physics, State Key Laboratory of Low-Dimensional Quantum Physics, Tsinghua University, Beijing 100084, P. R. China; and Frontier Science Center for Quantum Information, Beijing 100084, P. R. China,
E-mail: ycliu@tsinghua.edu.cn
Lingfeng Ou, State Key Laboratory of Low-Dimensional Quantum Physics, Tsinghua University, Beijing 100084, P. R. China,
E-mail: olf20@mails.tsinghua.edu.cn
Yuechen Lei, Beijing National Laboratory for Condensed Matter Physics, Institute of Physics, Chinese Academy of Sciences, Beijing 100094, P. R. China; and University of Chinese Academy of Sciences, Beijing 100049, P. R. China, E-mail: leiyuechen@iphy.ac.cn

1 Introduction

The field of optomechanics [1] studies the interaction between optical and mechanical degrees of freedom mediated by radiation pressure force. The use of optical microcavities can greatly enhance this optomechanical interaction. The field of cavity optomechanics has gained rapid development in the last two decades, originally spurred by the field of gravitational wave detection. Benefiting from the development of micro-/nano-fabrication techniques, various cavity optomechanical systems with both high optical and mechanical quality factors have been developed, for both fundamental research and practical applications. There have been several books [2, 3] and several excellent review papers [1, 4–6], focusing on the fundamental physics and quantum effects of cavity optomechanics. Researchers have used radiation pressure force of photons to control and manipulate motions of mechanical resonators to study the quantum mechanical effects of macroscopic mechanical resonators, such as to realize ground state cooling of macroscopic mechanical resonators [7–11], quantum squeezing of mechanical motions [12–15], and the production of squeezed light [16–18]. In addition, optomechanical induced transparency [19] and dark modes [20], strong coupling [21], and nonclassical correlations [22] between a mechanical resonator and an optical field, topological energy transfer [23], nonreciprocal control and cooling of mechanical modes [24], nonreciprocal transport of light [25–28], quantum entanglement between mechanical resonators [29, 30] have been realized in cavity optomechanical systems. Besides this intriguing fundamental research, cavity optomechanical systems also provide ideal platforms for precision sensing, due to the mechanical resonance enhanced response and optical resonance enhanced readout sensitivity. In contrast to traditional microelectromechanical systems (MEMS)-based sensing systems which use electric circuits to read out the signal, optical readout mechanism has less detrimental noise such as Johnson noise, and can easily reach quantum limited levels, known as shot noise. For instance, shot noise limited displacement sensitivity of the order of 10^{-19} m/$\sqrt{\text{Hz}}$ has been realized using cavity optomechanical systems [31]. Based on the ultrasensitive displacement measurement, precision sensing of various

physical quantities, such as force and mass, etc., has been realized. Besides the ultrahigh precision, cavity optomechanical sensors also provide the advantages of small size, low weight, and low power consumption, on-chip integration capability, compatibility with fiber coupling, etc., and therefore have great potential to be used in real applications in the near future. There have also been several review papers focusing on the applications of cavity optomechanics [32, 33]. Since then, the field of optomechanical applications has been rapidly developed, especially in the area of precision sensing. While this review will focus on the recent research progresses of optomechanical-system-based precision sensing applications, including displacement sensing [31], mass sensing [34], force sensing [35], atomic force microscope (AFM) [36–38] and magnetic resonance force microscope (MRFM) [39–41], accelerometry [42, 43], magnetometry [44–53], and acoustic sensing [54–65].

2 Physical principles of cavity optomechanical sensing

In this section, we introduce the physical principles of cavity optomechanical sensing. First we introduce the optomechanical coupling principle, review the different optomechanical sensing platforms developed in the past few years, and then discuss the noise, sensitivity, and bandwidth of optomechanical sensing.

2.1 Optomechanical coupling

Optomechanical coupling describes a phenomenon that an optical radiation field interacts with the mechanical vibrational mode. For example, we focus on a F–P optomechanical system (Figure 1). The cavity fields exert radiation pressure on the movable mirror, which leads to the changes of both the resonance frequency and damping rate and of the mechanical modes. At the same time, the mechanical vibration of the spring modulates the position of the movable mirror, which changes the cavity length L and optical resonant frequency ω_c.

To precisely model the coupling process, we provide a full quantum theory of cavity optomechanical coupling below. Here, both the mechanical resonator and the cavity field are pictured as quantized bosonic fields. Beginning with the system Hamiltonian and taking the dissipation into account, the system dynamics can be described by quantum Langevin equations. Let us consider a typical cavity optomechanical system composed of a single optical

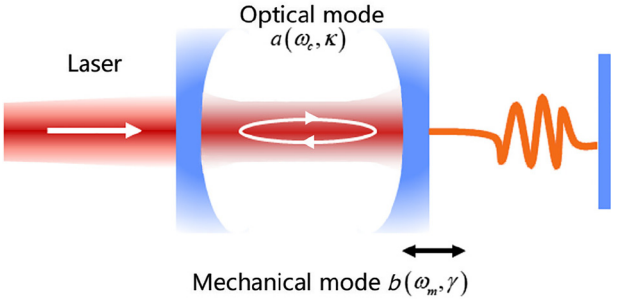

Figure 1: Schematic of a typical optomechanical system, with a laser-driven Fabry–Perot (F–P) cavity. The left mirror is fixed and the right mirror is movable.

cavity mode coupled with a mechanical mode, which can be modeled as a F–P cavity with one fixed mirror and one movable mirror mounted on a spring (Figure 1). The system's total Hamiltonian H can be written as

$$H = H_{\text{drive}} + H_{\text{free}} + H_{\text{int}}. \tag{1}$$

Here the first term of Eq. (1) (H_{drive}) describes the optical driving of the system. Consider that a continuous-wave laser is injected into the system, and the laser Hamiltonian is written as

$$H_{\text{drive}} = \Omega^* \, \mathrm{e}^{\mathrm{i}\omega_{\mathrm{L}} t} a + \Omega \, \mathrm{e}^{-\mathrm{i}\omega_{\mathrm{L}} t} a^\dagger, \tag{2}$$

where ω_{L} is the input laser frequency, a ($a^\dagger$) is the bosonic annihilation (creation) operator of the cavity optical mode, and $\Omega = \sqrt{\kappa_{\mathrm{ex}} P/(\hbar\omega_{\mathrm{L}})}\, \mathrm{e}^{\mathrm{i}\phi}$ denotes the driving strength, where P is the input laser power, ϕ is the initial phase of the input laser, and κ_{ex} is the decay rate of input-cavity coupling.

The second term of Eq. (1) (H_{free}) is the Hamiltonian of the uncoupled optical and mechanical modes, described by

$$H_{\text{free}} = \omega_{\mathrm{c}} a^\dagger a + \omega_m b^\dagger b. \tag{3}$$

Among it, the mechanical mode is regarded as a quantum harmonic oscillator, where b ($b^\dagger$) is the bosonic annihilation (creation) operator of the mechanical modes, and ω_{c} (ω_{m}) is the optical (mechanical) resonance frequency. The commutation relations satisfy $\left[a, a^\dagger\right] = 1$ and $\left[b, b^\dagger\right] = 1$. The displacement operator of the mechanical mode is given by $x = x_{\mathrm{ZPF}}(b^\dagger + b)$, where $x_{\mathrm{ZPF}} = \sqrt{\hbar/(2m_{\mathrm{eff}}\omega_{\mathrm{m}})}$ is the zero-point fluctuation, with m_{eff} being the effective mass of the mechanical mode.

The third term of Eq. (1) (H_{int}) describes the optomechanical interaction between the optical mode and the mechanical mode, which is given by

$$H_{\text{int}} = g a^\dagger a (b^\dagger + b). \tag{4}$$

Here $g = x_{\mathrm{ZPF}}G$ represents the single photon optomechanical coupling strength, and $G = \partial\omega_{\mathrm{c}}(x)/\partial x$ is the optomechanical coupling strength representing optical frequency shift per displacement. This Hamiltonian can be obtained by simply considering that the optical resonance frequency is modulated by the position of the mechanical resonator and using Taylor expansion at the original point, which is written by $\omega_{\mathrm{c}}(x) = \omega_{\mathrm{c}}(0) + x\partial\omega_{\mathrm{c}}(x)/\partial x + O(x) \simeq \omega_{\mathrm{c}}(0) + g\left(b^{\dagger} + b\right)$. A more rigorous and detailed derivation of this Hamiltonian can be found in Law's paper [66]. Besides, the radiation pressure force is written as the derivation of H_{int} with respect to displacement:

$$F = -\frac{\mathrm{d}H_{\mathrm{int}}}{\mathrm{d}x} = \frac{g}{x_{\mathrm{ZPF}}}a^{\dagger}a. \tag{5}$$

In the frame rotating at the input laser frequency ω_{L}, the system Hamiltonian is transformed to

$$H = -\Delta a^{\dagger}a + \omega_m b^{\dagger}b + ga^{\dagger}a\left(b^{\dagger} + b\right) + \left(\Omega^{*}a + \Omega a^{\dagger}\right), \tag{6}$$

where $\Delta = \omega_{\mathrm{L}} - \omega_{\mathrm{c}}$ is the input-cavity detuning.

The quantum Langevin equations are given by

$$\dot{a} = \left(\mathrm{i}\Delta - \frac{\kappa}{2}\right)a - \mathrm{i}ga\left(b + b^{\dagger}\right) - \mathrm{i}\Omega - \sqrt{\kappa_{\mathrm{ex}}}a_{\mathrm{in,ex}} - \sqrt{\kappa_0}a_{\mathrm{in},0}, \tag{7a}$$

$$\dot{b} = \left(-\mathrm{i}\omega_m - \frac{\gamma}{2}\right)b - \mathrm{i}ga^{\dagger}a - \sqrt{\gamma}b_{\mathrm{in}}. \tag{7b}$$

Here κ_0 is the intrinsic cavity decay rate, $\kappa = \kappa_0 + \kappa_{\mathrm{ex}}$ is the total cavity decay rate, γ is the damping rate of the mechanical mode. Besides, $a_{\mathrm{in},0}$, $a_{\mathrm{in,ex}}$, and b_{in} are the noise operators associated with the intrinsic cavity decay, external cavity decay(input-cavity coupling), and mechanical damping. Additionally, the quality factors of optical and mechanical mode are defined as the ratio of their resonant frequency and damping rate respectively, which are $Q_{\mathrm{o}} = \kappa/\omega_{\mathrm{c}}$ and $Q_{\mathrm{m}} = \gamma/\omega_{\mathrm{m}}$.

The optomechanical coupling enables optical readout of mechanical motions. As shown in Figure 2A, when the laser frequency $f_{\mathrm{L}} = \omega_{\mathrm{L}}/2\pi$ is locked on the side of an optical resonance, the mechanical oscillation with a displacement of x translates into a periodic change in the cavity length, and therefore shifts the optical resonance frequency and modulates the amplitude of the intracavity field periodically. As a result, the output photocurrent $i(t)$ experiences a periodic modulation, with a frequency corresponding to the mechanical frequency ω_{m}, and an amplitude proportional to the displacement x and

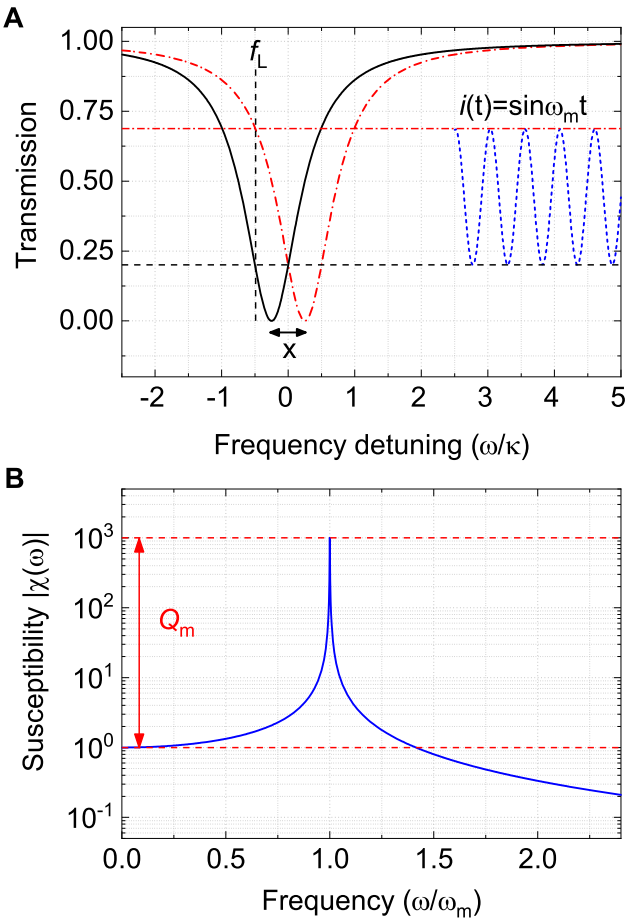

Figure 2: (A) Physical principle of optical readout of the mechanical motion. A mechanical displacement x shifts the optical transmission spectrum from the black solid curve to the red dash-dotted curve. The periodic mechanical motion therefore cause a modulation of the output photocurrent $i(t)$, when the laser frequency f_{L} is locked on the side of the optical resonance. (B) Susceptibility $|\chi(\omega)|$ of a mechanical resonator as a function of the frequency, normalized to its zero frequency susceptibility $|\chi(0)|$. The susceptibility on the mechanical resonance is enhanced by a factor of mechanical quality factor Q_{m} compared to that at zero frequency.

linearized optomechanical coupling strength G. For simplicity, we consider a simple case of a single mechanical resonance, for which the response of a mechanical resonator to an external force as a function of the frequency is quantified by the mechanical susceptibility of the resonator $\chi(\omega) = 1/(m_{\mathrm{eff}}(\omega_{\mathrm{m}}^2 - \omega^2 - \mathrm{i}\omega\gamma))$. In Figure 2B we plot $|\chi(\omega)|$ of a mechanical resonator with mechanical quality factor $Q_{\mathrm{m}} = 1000$, normalized to the susceptibility at zero frequency $|\chi(0)|$. It can be seen that the response of a mechanical resonator to external force is significantly enhanced at its mechanical resonance, with a factor of Q_{m}. Therefore, the mechanical response to an external stimulus, such as force and acoustic pressure,

etc., is enhanced by the mechanical resonance, and having a high mechanical quality factor is important to achieve better measurement sensitivity. In addition, the optical read-out sensitivity is also enhanced by the optical resonance, benefitting from the ultrahigh optical quality factor of the microcavities.

2.2 Optomechanical sensing platforms

With the development of micro-/nano-fabrication techniques, various optomechanical platforms have been developed, including macroscopic and microscale suspended mirrors, membranes, waveguides, cantilevers, whispering gallery mode (WGM) microresonators and photonic crystal cavities. Among them, WGM microresonators and photonic crystal cavities have attracted increasing research interests for precision sensing applications, due to their high Q optical and mechanical resonances, good optomechanical coupling, and capability for integration. This review will mainly focus on optomechanical sensing using WGM microcavities and photonic crystal cavities.

From the viewpoint of geometrical optics, WGM microresonators [75] confine light through total internal reflection of light along the inner surface of a rotational symmetric resonator. Due to their extremely high optical Q_0 factors and small mode volumes, WGM microresonators have been found various applications in quantum electrodynamics, quantum optics, ultrasensitive sensing, low threshold microlasing, nonlinear optics, and cavity optomechanics, etc. Various types of WGM microresonators have been developed for optomechanical sensing applications, including microspheres, microbottles, microbubbles, microrods, microdisks, microtoroids, microrings, etc. Microspheres were the earliest type of WGM microresonator researchers used, which can be easily fabricated by melting the tips of optical fibers. For example, a silica microsphere has been used to detect a single molecule (Figure 3A), through monitoring the mechanical frequency shift induced by molecule binding [67]. They have ultrahigh optical Q_0 factors (typically larger than 10^8). In order to achieve on-chip integration, researchers later developed silica microdisks that can be massively

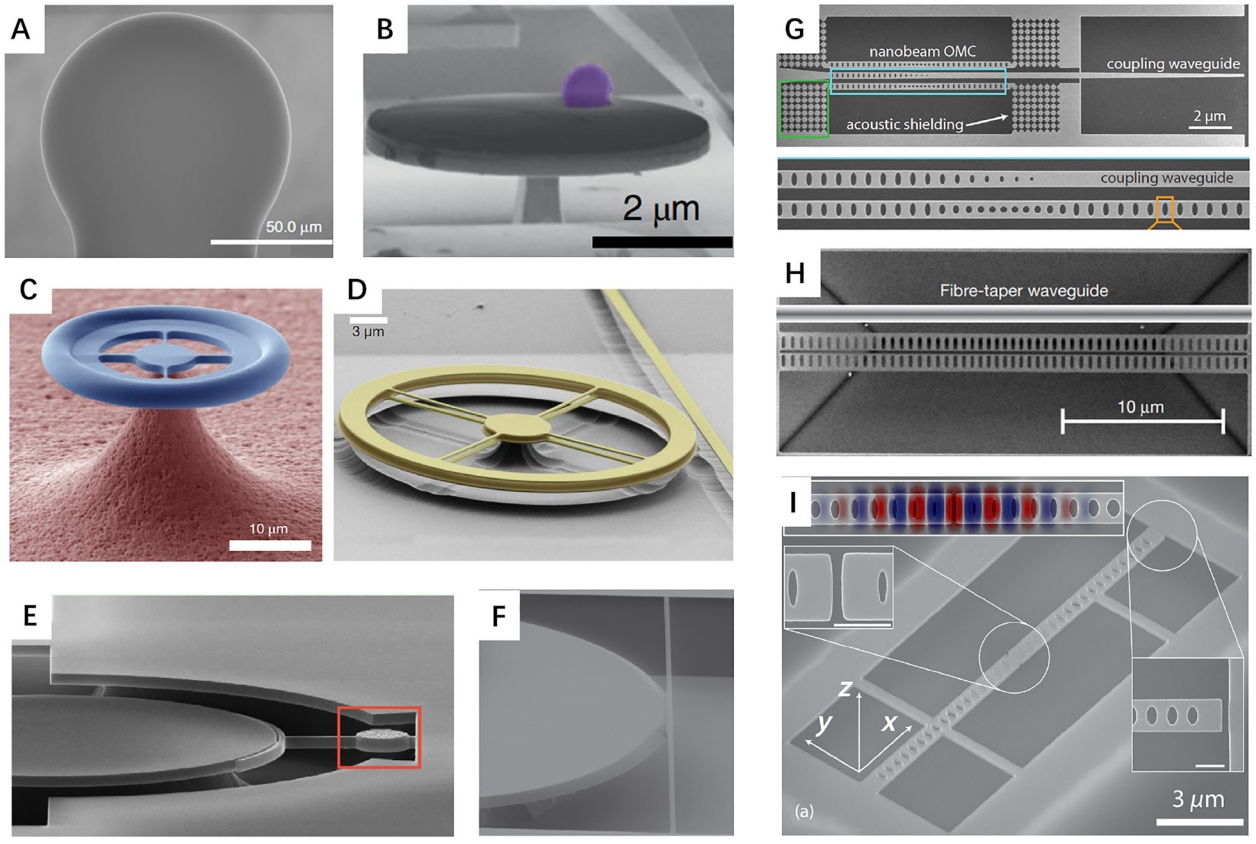

Figure 3: Various optomechanical sensing platforms. (A)–(D) Are whispering gallery mode microresonators: (A) silica microsphere [67]. (B) GaAs microdisk [68]. (C) Silica microtoroid [69]. (D) Silicon nitride double disks [70]. (E) Microcantilever mechanical resonator coupled with a microdisk cavity [71]. (F) Nanostring mechanical resonator coupled with a microdisk cavity [35]. (G)–(I) are photonic crystal nanomechanical resonators, including single photonic crystal nanobeam cavities (G) [72], two coupled photonic crystal nanobeam cavities (H) [73], split coupled photonic crystal nanobeam cavities (I) [74].

fabricated on a silicon chip through photolithography. In recent years, microdisks based on various material systems have been developed, such as GaAs, silicon nitride, crystalline, and polymer microdisks, etc. For example, a GaAs microdisk with mechanical resonances at a few hundreds of MHz has been used to measure the mechanical oscillation of a single bacterium (Figure 3B) [68]. In order to decrease the surface roughness of the silica microdisks, the Vahala group developed a CO_2 laser reflow technique which can melt the edge of the microdisks into microtoroids, and can significantly increase the optical Q_o factors to 10^8 level [76]. Ultralow dissipation and therefore high mechanical quality factors (higher than 50,000) have been realized in spokes supported microtoroids, as the clamping loss can be significantly reduced (Figure 3C) [69, 77]. These spoked microtoroids can be functionalized with electrodes for optical tuning or electric field detection [78]. Double disk microresonators [70, 79–83] have also been fabricated, which consist of two parallel silica or silicon nitride microdisks separated by a few hundred nanometers in the vertical directions (Figure 3D). These double disk microresonators support WGM optical modes shared by the two disks and mechanical modes in which two disks move towards opposite directions (flapping modes). The mechanical motion of the flapping mode shifts the optical resonance sensitively, with optomechanical coupling strength of several tens of GHz/nm, which is typically one order of magnitude higher than the radial breathing mode in a single disk. Therefore these double disk microresonators provide an ideal platform for optomechanics research. These double disk microresonators can also be functionalized with gold electrodes for electrical tuning of optical resonances or electric field sensing [83].

Due to their high optical Q_o factors, WGM optical microresonators can also be used to read out motions of external mechanical resonators. For example, a microtoroid cavity is used to evanescently read out the mechanical motions of a silicon nitride nanobeam [84]. A microfork mechanical resonator coated with a magnetic material coupled with a silicon microdisk cavity has been fabricated as a torque sensor, which can measure the magnetic moment of the magnetic material (Figure 3E) [71, 85]. In this coupled system, the mechanical resonator experiences a torque acted on the magnetic material by an external magnetic field, and the mechanical motion can be optically read out with high sensitivity using the microdisk resonator. In addition, a silica microdisk and silicon nitride nanobeam mechanical resonator integrated on the same chip has been realized for ultrasensitive sensing (Figure 3F) [35]. High-Q_o microtoroidal resonators have also been used to detect the surface wave motion of a thin film of superfluidic Helium [86]. Very recently, superfluidic helium droplet which supports both optical WGM modes and mechanical modes has also been used for optomechanics study [87]. These superfluidic optomechanical systems have the potential for precision rotation sensing.

Another type of high Q_o optical cavity is photonic crystal cavities. They confine light within a defect area in a periodic dielectric structure by photonic bandgap. Due to their high Q_o factors, extremely small mode volumes, typical on the order of λ^3 with λ being the wavelength), and ease of integration, photonic crystal cavities have also attracted increasing research interest. These photonic crystal cavities also support high Q_m mechanical resonances, and therefore provide an ideal platform for optomechanical sensing. Optomechanical crystals were first developed by the Painter group in 2009 [88], and the optomechanical crystal with mechanical Q_m factor as high as 10^{10} has been realized in 2020 [72], by carefully designing the phononic bandgap structure (Figure 3G). Coupled optomechanical crystals have also been realized, with high optomechanical coupling strength (Figure 3H) [73]. A split photonic crystal cavity (Figure 3I) [74] and a hetero photonic crystal cavity [89] have also been realized for magnetic field sensing and mass sensing, respectively.

2.3 Noise, sensitivity, and bandwidth

The most important parameter for optomechanical sensors is sensitivity, which is defined as the minimum detectable signal, and can be quantified by the noise equivalent signal. Thus we will discuss the noise sources in the optomechanical systems, which include thermal noise from the thermal environment with nonzero temperature, and noises from the probe laser. Noises from the probe lasers consist of the classical noise and the quantum noise. The classical noise (mainly in the low frequency range) includes laser intensity noise, phase noise, etc., which can be suppressed by some measurement techniques, such as balanced homodyne detection. The quantum noise originates from the quantum property of photons, also known as photon shot noise. In optomechanical systems, the quantum noise includes the imprecision noise and the backaction noise. The imprecision noise originates from the uncertainty relation between the number and the phase of photons, while the backaction noise (or radiation pressure noise) originates from the radiation pressure force of photons acting on the mechanical resonator. In most cases of optomechanical sensing applications, the probe laser power is relatively low, to avoid thermal effect induced optical resonance shift [48], and thus the backaction noise

is typically negligible. As a result, here we mainly consider the thermal noise and shot noise in the optomechanical sensing systems.

The sensitivity of a physical quantity A (including displacement, force, etc.) at the frequency ω is determined by $\sqrt{S_{AA}(\omega)}$, where the noise spectrum is defined as the Fourier transform of the autocorrelation function of A as $S_{AA}(\omega) = \int_{-\infty}^{+\infty} \langle A(t) A(0) \rangle e^{i\omega t} dt$ Microtoroids have high optical quality factors and broad mechanical resonance frequency range, therefore providing a good platform for high sensitivity and broad bandwidth optomechanical sensing. Here we consider a microtoroid mechanical optomechanical resonator, with an optical quality factor $Q_o = 10^6$, mechanical quality factor $Q_m = 1000$, effective mass $m_{eff} = 2$ ng, optomechanical coupling strength $G = 500$ MHz/nm. At room temperature $T = 300$ K, a mechanical resonator experiences a thermal noise force $F_{th} = \sqrt{S_{FF}(\omega)} = \sqrt{2m_{meff}\gamma k_B T}$ [1]. The displacement noise power spectrum of a mechanical resonator from thermal noise is

$$S_{xx}^{th}(\omega) = |\chi(\omega)|^2 F_{th}^2 = \frac{2\gamma k_B T}{m_{eff}\left[\left(\omega_m^2 - \omega^2\right)^2 - \omega^2\gamma^2\right)\right]}, \quad (8)$$

as shown in the black solid curve in Figure 4A. It exhibits a peak on the mechanical resonance and decays rapidly away from the mechanical resonance. The displacement noise power spectrum from the laser shot noise, on the other hand, is frequency independent [2].

$$S_{xx}^{shot}(\omega) = \frac{\kappa}{16\eta N g_0^2}\left(1 + \frac{\omega^2}{\kappa^2}\right), \quad (9)$$

where κ is the total optical decay rate, $\eta = 0.8$ is the optical detection efficiency, N is the intracavity photon number $N = P\kappa_{ex}/(\hbar\omega_L)$ for probe power P. The displacement noise power spectra for shot noise at different powers are shown in the black (200 μW), red (2 μW), blue (20 nW), purple (200 pW), and green (2 pW) dotted curves. The total noise power spectra for displacement at different powers are shown in the dash-dotted curves. It can be seen that, the systems have less noise at off-resonance frequency. And as the probe power increases, the shot noise dominated displacement sensitivity is improved and thermal noise limited displacement sensitivity is easier to reach for high probe power cases. In addition to the probe power, the optical Q_o factor and optomechanical coupling strength also affect the sensitivity. The higher Q_o and G are, the higher the readout sensitivity is, and therefore it is easier to reach thermal noise limited sensitivity.

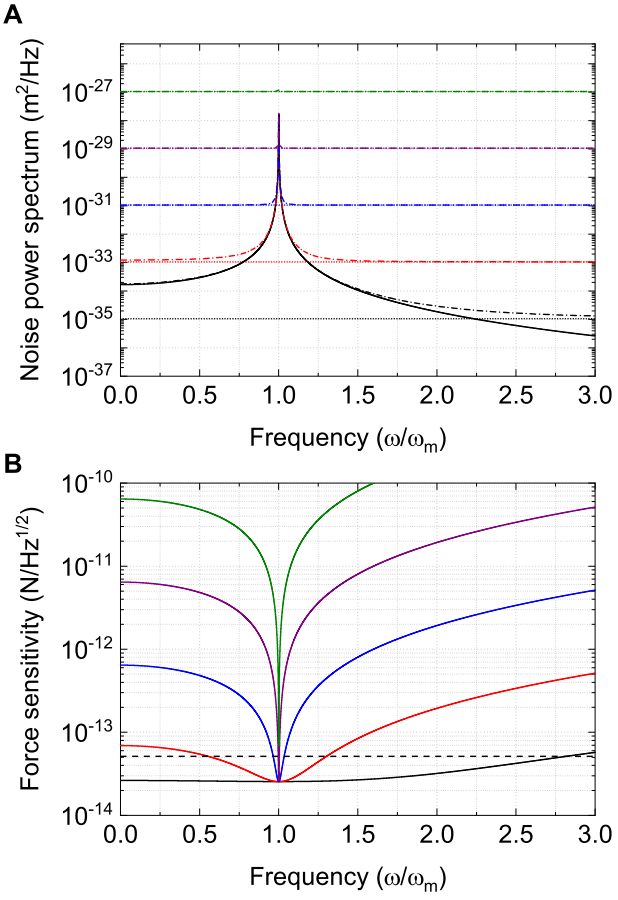

Figure 4: (A) Displacement noise power spectra of a mechanical resonator. The black solid curve denotes the thermal noise. The dotted lines denote shot noise at different powers: 200 μW (black), 2 μW (red), 20 nW (blue), 200 pW (purple), and 2 pW (green), respectively. The dash-dotted curves are total noise at different powers: 200 μW (black), 2 μW (red), 20 nW (blue), 200 pW (purple), and 2 pW (green), respectively. (B) Force sensitivity as a function of the frequency, for different powers corresponding to those in (A).

Practical optomechanical sensors are usually used to detect an external physical quantity. For example, for magnetic field sensing using optomechanical systems, it is essentially detecting a magnetic field (B) induced force ($F \propto B$) acting on the mechanical resonator. Therefore in the following, we discuss the force sensitivity $\sqrt{S_{FF}(\omega)} = \sqrt{S_{xx}(\omega)}/|\chi(\omega)|$ of a mechanical resonator. In Figure 4B, we plot the force sensitivity as a function of the frequency, for different probe powers. It can be seen that the peak sensitivity for force occurs at the mechanical resonance frequency, and the sensitivity degrades when going away from the mechanical resonance. As a result, reaching thermal noise limited regime is beneficial for better sensitivity. The peak sensitivity is dependent on the mechanical damping rate gamma. Therefore, having a lower damping rate

(or higher mechanical Q_m factor) is important for a better force sensitivity.

In order to characterize the frequency dependent sensitivity, we define a bandwidth as the frequency range in which the sensitivity is better than twice of the peak sensitivity (below the dashed line in Figure 4B). It can be seen that, the higher the probe power is, the broader the bandwidth is. For example, at a probe power of 200 μW, the thermal noise limited frequency range covers all the way from DC to about twice the resonance frequency. In addition to probe power, having a higher optical factor Q_o and optomechanical coupling strength are also helpful to reach the thermal noise limited sensitivity, and therefore broadening the bandwidth of the optomechanical force sensor. This means that optomechanical sensors provide an ultrabroadband sensing platform, with bandwidth easily reaching tens of MHz.

3 Optomechanical sensing applications

3.1 Displacement sensing

Ultrahigh-sensitivity displacement sensing is the core of precision detection of many physical quantities, such as force (Section 3.3), magnetic field (Section 3.5), acceleration (Section 3.6) and ultrasound (Section 3.7). Thanks to the strong coupling between the optical cavity and the mechanical resonator, the optomechanical system provides an excellent platform for precision displacement sensing.

The displacement sensing based on the optomechanical system (Figure 1) is to measure the displacement $x(\omega)$ of the mechanical resonator in the frequency domain. In general, through optomechanical coupling, the optical transmission signal carries the information of the displacement of the mechanical resonator. Then, it can be read out by a photodetector and optical spectrum analyzers [32].

Various cavity optomechanical systems have been demonstrated to be suitable for the displacement sensors, involving WGM cavities [8, 31, 84, 90, 92], photonic crystal cavities [73, 93, 95, 96], F–P cavities [97]. Table 1 summarizes the relevant optomechanical parameters for some representative recent experimental implementations in displacement sensing.

The displacement sensor based on WGM cavity optomechanical systems has been demonstrated to possess high sensitivity. In 2008, Schliesser et al. reported a displacement sensor based on a silica microtoroid cavity optomechanical system (Figure 5). They reduced the noise by utilizing homodyne and polarization spectroscopy techniques and achieved the displacement sensitivity of 10^{-19} m/$\sqrt{\text{Hz}}$ level, which was limited by the shot noise [31]. In 2010, Ding et al. developed a microdisk made of GaAs. Due to the high refractive index of GaAs, the optomechanical coupling G reached 71 GHz/nm, which led the sensitivities of their system down to 2×10^{-17} m/$\sqrt{\text{Hz}}$ [90].

Apart from coupling with the internal mechanical mode, the WGM microcavities were also explored to couple with the external mechanical resonators through the

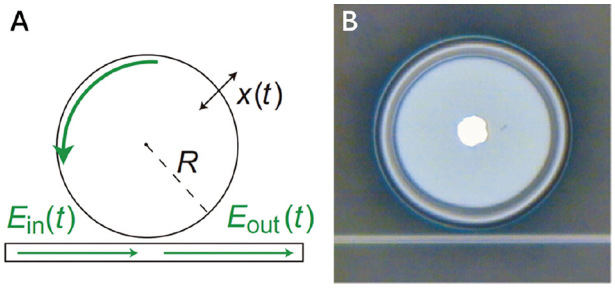

Figure 5: Motion transduction with a microtoroid cavity. (A) Schematic and (B) optical microscope image of tapered fiber coupled microtoroid cavity [31].

Table 1: Experimental parameters for a representative sampling of published displcement sensors experiments.

Device type	$\sqrt{S_{xx}}(m/\sqrt{\text{Hz}})$	m_{eff} (kg)	Q_m	G (MHz · nm^{-1})	Year
1. Microtoroid [31]	$\sim9.0\times10^{-19}$	1.0×10^{-11}	$>5.0\times10^{4}$	–	2008
2. Microdisk [90]	2.0×10^{-17}	2.1×10^{-14}	6.6×10^{2}	7.1×10^{4}	2010
3. Microtoroid cavity-string [84]	5.7×10^{-16}	4.9×10^{-15}	4.0×10^{4}	2.3×10^{1}	2009
4. Microtoroid cavity-nanowire [91]	5.3×10^{-16}	4.0×10^{-15}	2.8×10^{2}	9.4×10^{1}	2010
5. Microdisk cavity-nanobeam [92]	4.3×10^{-17}	2.9×10^{-15}	7.6×10^{5}	4.4×10^{3}	2015
6. Photonic crystal nanobeam [73]	5.0×10^{-17}	4.3×10^{-14}	$(0.5\sim1.5)\times10^{2}$	7.7×10^{5}	2009
7. Photonic crystal nanobeam [42]	4.0×10^{-15}	1.0×10^{-11}	1.4×10^{6}	3.5×10^{4}	2012
8. Photonic crystal nanobeam [93]	9.3×10^{-18}	1.4×10^{-16}	6.6×10^{0}	7.8×10^{5}	2017
9. Microwave cavity-nanowire [94]	4.8×10^{-15}	1.1×10^{-14}	6.2×10^{5}	2.0×10^{-1}	2009

near field. The superiority of the evanescent field coupling is separating the optical and mechanical degrees of freedom, which extends the sizes of the measured mechanical resonator into the nanoscale. In 2009, Anetsberger et al. put forward a displacement detector based on the near-field cavity optomechanics (Figure 6A). They measured the motion of the external SiN strings employing the evanescent field of the toroid silica microcavities. Taking advantage of a Pound–Drever–Hall (PDH) technique [97], they implemented the sensitivity of 5.7×10^{-16} m/$\sqrt{\text{Hz}}$, limited by the shot noise [84]. In 2015, Wilson et al. exploited the special fabrication technique to significantly shorten the distance between the mechanical and optical elements, which enhanced the optomechanical coupling to $G = 4.4$ GHz/nm. Assisted by the feedback cooling method, the sensitivity of their system was down to 4.3×10^{-17} m/$\sqrt{\text{Hz}}$, which was a combination of thermorefractive noise, diode laser frequency noise, and so on [92].

From works 2, 3, 4, 5 in Table 1 and Eq. (9), it is seen that increasing the optomechanical coupling helps enhance the shot-noise-limited displacement sensitivity. Benefiting from the strong optomechanical coupling (G above 10 GHz/nm), the factor limiting the sensitivity of photonic crystal cavity systems is no longer shot noise. In 2009, Eichenfield et al. proposed a displacement sensor based on the Si_3N_4 photonic crystal cavities. Limited by the photoreceiver noise, their system got the sensitivity with 5×10^{-17} m/$\sqrt{\text{Hz}}$ [73]. In 2017, Zhang et al. demonstrated a detection system with a femtogram scale nanobeam optomechanical crystal resonator. Even in the water, its sensitivity achieved 9.3×10^{-18} m/$\sqrt{\text{Hz}}$ [93], in the same year, Zobenica et al. presented an integrated sensor utilizing the photonic crystal cavity (Figure 7). As Figure 7B showed, the tuning, sensing, and read-out functions were concentrated in an area of only $15 \times 15 \mu m^2$. Employing an electromechanically tunable, double-membrane

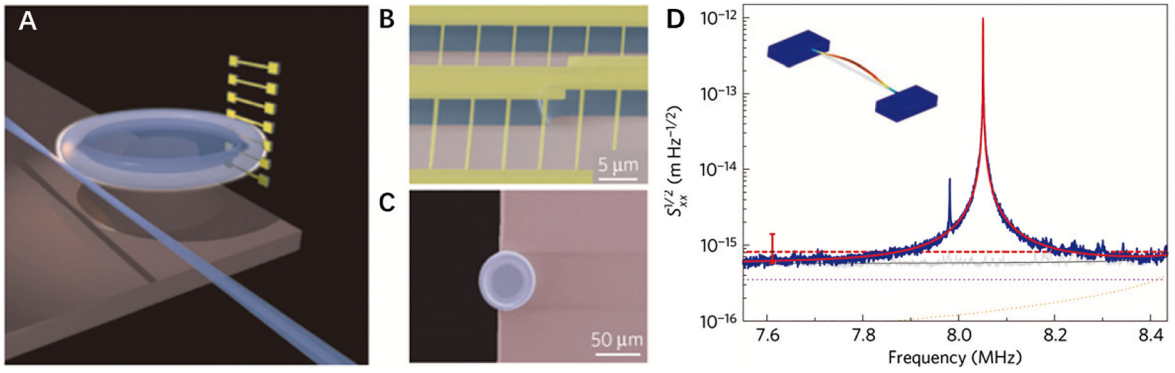

Figure 6: (A) Schematic of the tapered-fiber-interfaced optical cavity dispersively coupled with an array of nanomechanical resonators. Scanning electron micrograph (false color) of (B) doubly clamped SiN nanostring resonators and (C) microtoroid cavity. (D) Displacement density as a function of frequency. Inset: finite-element simulation of the string's fundamental mode [84].

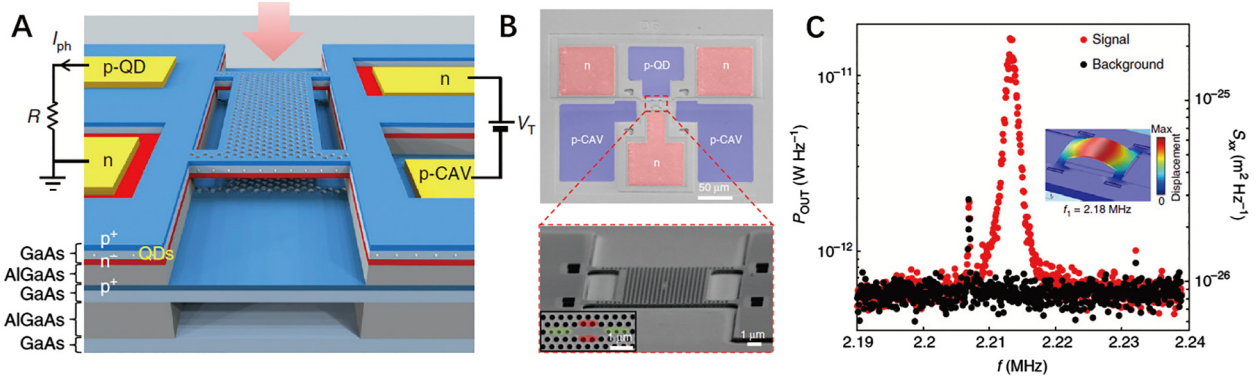

Figure 7: (A) Sketch of the photonic crystal cavity sensing device. (B) False-colored SEM image of a typical device (top view) with contact pads to both sensing and actuation diodes. Bottom: zoom-in SEM image showing the active part of the sensor: a four-arm bridge structure containing a photonic crystal cavity suspended above a fixed photonic crystal membrane. Inset: SEM image of the patterned optical cavity. (C) Electronic spectrum analyzer spectrum of the photocurrent noise where the fundamental mechanical mode is visible in the output power (red dots) and control measurement with laser off (black dots). The right axis displays the calibrated power spectral density of motion. Insert: finite-element simulation of fundamental mechanical mode at frequency of 2.18 MHz [95].

photonic crystal cavity, the system had a sensitivity of 1×10^{-13} m/$\sqrt{\text{Hz}}$ restricted by the pick-up electrical noise [95]. Then, in 2020, Galeotti et al. rolled off the sensitivity of the on-chip displacement sensor to 7×10^{-15} m/$\sqrt{\text{Hz}}$, which was helped by using more compact electrical probes with correspondingly lower pick-up noise [96].

In addition to the above examples, there are other schemes to realize displacement sensing in optomechanical systems. In 2013, Tallur et al. illustrated a detection approach based on Rayleigh scattering in an optomechanical system, which enhanced the displacement sensitivity at multi GHz frequencies in the resolved sideband regime [98]. Then in 2020, Liu et al. proposed an integrated cavity-free optomechanical displacement sensor, which was based on a three-dimensional directional coupler and dual-channel waveguide photodiodes. Constrained by the pick-up electric noise, their system attained the sensitivity of 4.5×10^{-14} m/$\sqrt{\text{Hz}}$ [99].

Grounded on quantum correlations between the shot and backaction noise, there are some works in reducing the quantum noise and even obtaining the displacement sensitivity beyond the standard quantum limit (SQL) [1]. In 2013, Hoff et al. demonstrated that injecting the squeezed light helps reduce the shot noise in the microcavity system [100]. In 2015, Peano et al. provided a scheme of creating squeezed light inside the cavity with a nonlinear medium, which enhanced the signal-to-noise ratio (SNR) of the system [101]. In 2017, Kampel et al. modified the readout of the interferometer, also called variational techniques, and realized the near-SQL-limited measurement [102]. In 2019, Mason et al. improved the variational techniques and realized the beyond-SQL sensitivity at the off-resonant frequency [103]. In 2020, Sainadh et al. put forward a scheme of beating the SQL through the interaction between the linear and quadratic optomechanical coupling in an unresolved sideband limit [104].

3.2 Mass sensing

Traditionally, the mass of tiny charged particles is measured by the mass spectrometer [105]. Due to the need for the measurement of molecular-scale substances in the fields of chemistry and biology, the measurement of the mass of electrically neutral particles has become a hot research issue [106]. In general, the minuscule size of microresonators renders their physical properties extremely sensitive to the perturbation caused by external influence. These mechanical resonator-based mass sensors rely on a resonant frequency shift due to an accreted mass and do not need the process of molecular ionization, opening a new chapter during these years in the field of nanotechnology measurement. At present, there are two methods for microresonator frequency measurement, the electrical measurement method [107, 108] and the optical measurement method [109, 110]. This section will introduce the latter in detail.

The resonator acts as a mass sensor due to the resonance frequency sensitivity of the mass absorbed onto it. Although the measurement technique is quite challenging, the principle of mass sensing is still simple. A mechanical resonator can be described by a harmonic oscillator, which has an effective mass m_{eff}, a spring constant k, and a resonance frequency

$$f_{\text{m}} = \frac{1}{2\pi}\sqrt{\frac{k}{m_{\text{eff}}}}. \tag{10}$$

Changes in the spring effective mass δm_{eff} will cause the resonance frequency shift of the mechanical resonator δf_{m}, which is $\delta m_{\text{eff}} = 2m_{\text{eff}}\delta f_{\text{m}}/f_{\text{m}}$. Qualitatively, we simply consider the deposited mass as

$$m_{\text{d}} \approx \delta m_{\text{eff}} = -\frac{2m_{\text{eff}}}{f_{\text{m}}}\delta f_{\text{m}}. \tag{11}$$

It can be seen from Eq. (11) that when the resolution of the instrument is fixed, smaller masses can be detected by reducing the effective mass of the mechanical resonator or increasing the resonance frequency of the mechanical resonator. More specifically, the relationship between deposition mass and the frequency shift also depends on the binding position of the object in the mechanical mode [111, 112].

In 2012, Li et al. proposed a scheme of the all-optical mass sensor based on an optomechanical system, in which a microtoroid cavity was coupled to a strong pump field

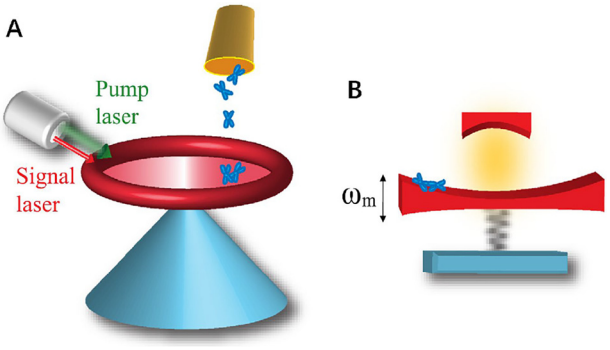

Figure 8: Diagram of the all-optical mass sensor based on an optomechanical system. (A) A strong pump field and a weak signal field are applied to a toroidal nanocavity system, which weighs the masses of biological chromosome. (B) Equivalent figure of (A) in the typical cavity optomechanical system, which consists of a movable mirror connected with a spring and a fixed mirror [113].

and a weak signal field [113], as shown in Figure 8. Later, in 2013, Liu et al. realized the mass sensor in silica microtoroid cavity optomechanical systems Figure 9. Due to the resonator with 6.0×10^{-8} g effective mass and 1.5×10^{3} effective mechanical quality factor, the system exhibited 150 fg (1.5×10^{-13} g) mass sensitivity. As Figure 9A shows, the driving light provided by near-infrared (IR) tunable laser acted as both pump source and probe light, which were coupled into and out of the microtoroidal cavity utilizing a silica fiber taper. The pump power exceeds the optomechanical oscillation threshold, and the probe light optical signal was transferred into the electrical signal that was collected and analyzed in the RF spectrum analyzer. Frequency shifts of the microtoroid as adding microbeads with different mass are shown in Figure 9C. Figure 9F is the RF spectrum of the fundamental optomechanical vibration in 8.505 MHz and its high-order harmonics. Furthermore, they demonstrated intrinsic harmonic optical modulation inside the optomechanical system can amplify the signal to enhance the sensitivity of the system [109].

In 2016, Yu et al. developed a microsphere cavity optomechanical system (Figure 10), whose mechanical resonator had 10^{-6} g effective mass and 2.6×10^{6} effective mechanical factor, leading to 66 kDa (1.1×10^{-19} g) mass sensitivity. Figure 10B is the power spectral density of the cavity transmission displaying the 262 kHz fundamental oscillation and its high-order harmonics. They put the microspheres into the solution of the protein molecule and observed the binding event of the protein molecule and microspheres by the recorded time-frequency diagram of the system under the third harmonic of the oscillation frequency. As shown in Figure 10C, the binding and separation of protein molecules with microspheres were observed at the time of 28 and 34 s, respectively [110]. Their works showed the excellent performance of the microsphere cavities in the liquid environment as well as the potential of the optomechanical system in the detection of biomolecules.

Additionally, there are also theoretical schemes to explore ways to improve sensitivity or propose new systems. One way to reduce the mechanical linewidth is to use a double cavities optomechanical system. In 2014, Jiang et al. proposed a scheme based on the hybrid opto electromechanical systems, where an optical cavity and a superconducting cavity coupled with a mechanical resonator at the same time [114]. Soon afterward, in 2015, they illustrated an approach that utilizes the coupled two microtoroid cavities optomechanical system, whose bandwidth was nearly 1/14 of the one in the single cavity system [115]. In 2017, Lin et al. demonstrated a method to reduce the environmental noises in mass sensing by detecting the change of cavity quadratures for optomechanical systems [116]. In 2018, Liu et al. proposed an optical weighing technique. The optomechanical system was composed of a plasmonic cavity and a suspended graphene nanoribbon with a tiny mass, a high mechanical frequency, and a narrow mechanical bandwidth, which was predicted to have sensitivity down to a single atom [117]. Then, in 2019, Liu et al. illustrated a scheme embedding the degenerate

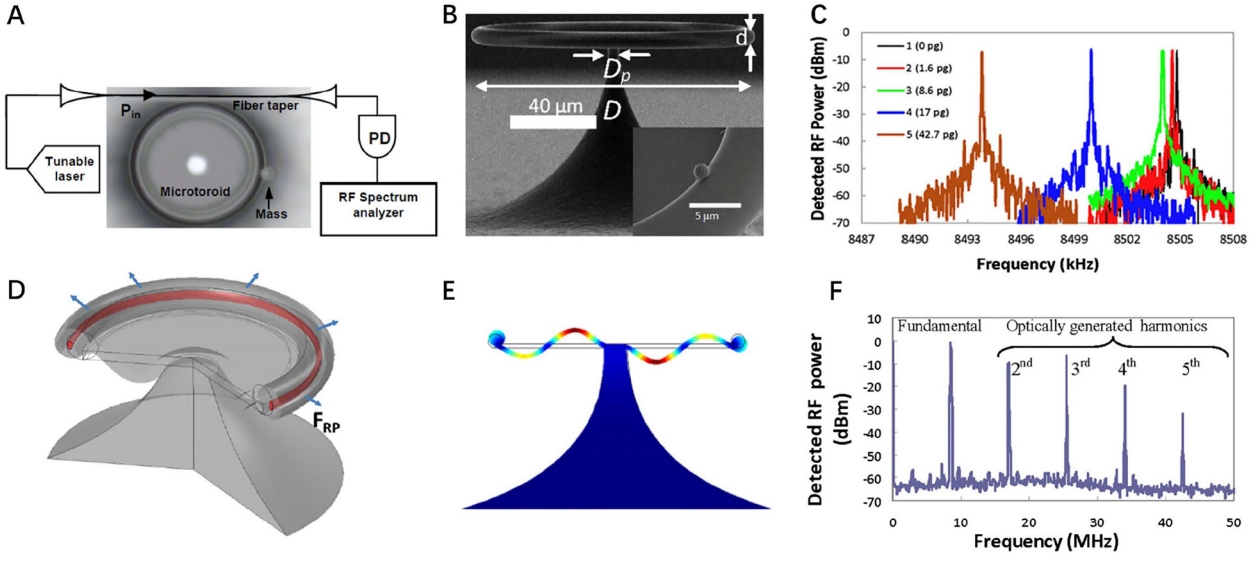

Figure 9: (A) Sketch of experimental setups for mass measurement using microtoroid optomechanical systems. (B) Scanning electron microscope (SEM) image of one of the utilized microtoroids. Inset: a polyethylene microbead landed on the toroidal region of the resonator. (C) Radio frequency (RF) spectrum near the fundamental frequency as adding microbeads with different mass. (D) Schematic diagram of radial breathing mode of microtoroids. (E) Finite-element simulation of modeling for displacements of one of the mechanical modes. (F) RF spectrum of the optical output power in the absence of the microbeads [109].

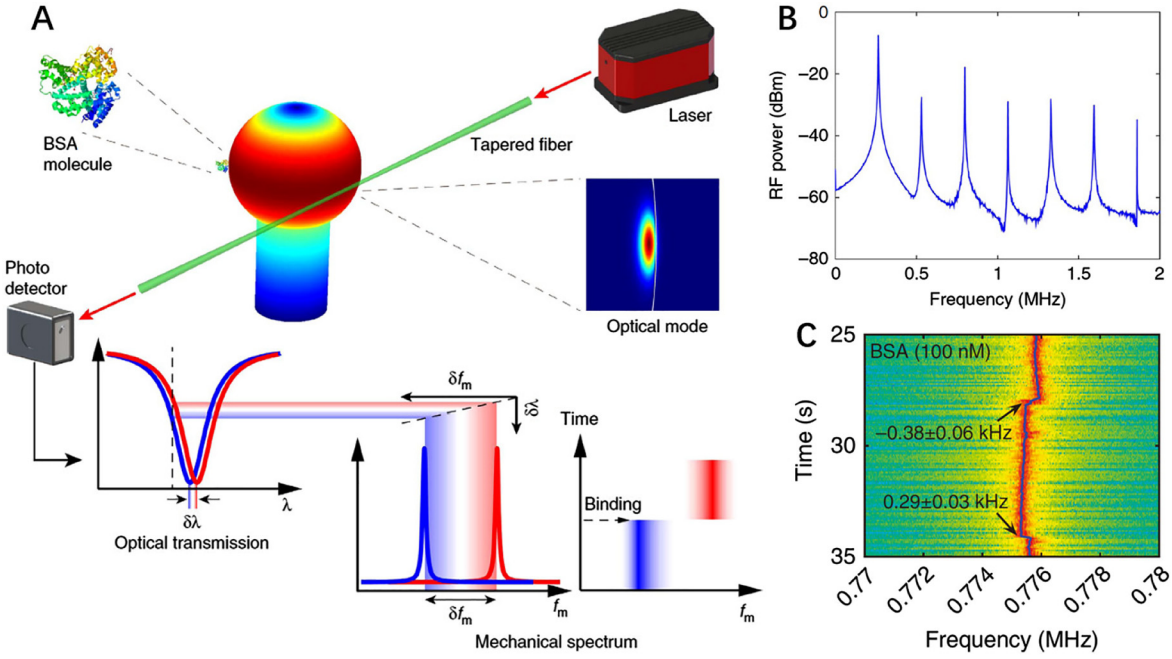

Figure 10: (A) Schematic illustrating the sensing mechanism. When binding the molecules, the optical transmission curve of the optomechanical system drifts from the red line into the blue line. The color map on the microsphere shows the radial breathing mechanical mode simulated by the finite element method. (B) The power spectral density of the cavity transmission. (C) Typical mechanical spectrograms recorded at the third harmonic of the oscillation tone with 100 nM-nominal-concentration protein molecules [110].

parametric amplifier into a membrane-in-the-middle cavity driven by a strong control field and a weak probe pulse. It amplified the detecting signal via a nonlinear second-order sideband process [118].

Nanomechanical mass spectrometry is well suited for the analysis of high mass species such as viruses. Previously used one-dimensional mechanical resonators have a disadvantage that the sensing signal is sensitively dependent on the binding position of the particles on the mechanical resonator. To overcome this problem, specific readout schemes can be used to simultaneously monitor multiple resonance modes, which make sensing more complicated. In 2020, Sansa et al. demonstrated single-particle mass spectrometry with nano optomechanical resonators fabricated with a very large scale integration process [34], which a uniform sensing signal for particles binding at different positions on the mechanical resonator.

The mass spectrometer uses a plate mechanical resonator coupled with a WGM microdisk cavity. The working principle of the mass spectrometry is as follows. Each time a particle with a mass m_p lands on the mechanical resonator, the mass of the mechanical resonator M_{res} changes by m_p, therefore its resonance frequency ω_m changes from $\sqrt{k/M_{res}}$ to $\sqrt{k/(M_{res}+m_p)}$. The resonance frequency of the mechanical resonator is optically read out by the microdisk evanescently. In order to eliminate the effect of the particle landing position, they use an in-plane vibration mode, with the mode profile shown in Figure 11. Figure 11B shows the finite-element color map of normalized frequency sensitivity to added point mass, showing that the frequency shift due to particle adsorption does not depend on particle position on the platform. Figure 11C shows the false-colored scanning electron microscope images of the device, general view (left), and zoom-in on the nanoram (right). The platform is 1.5 μm wide and 3 μm long, with 80 × 500 nm support beams. The optical ring diameter is 20 μm, and the optical ring-to-platform gap is 100 nm. Close to 1.55 μm wavelength light is coupled in and out of the ring by optical waveguides through a 200 nm gap. The silicon-on-insulator (SOI) top layer is 220 nm thick, partially etched to realize the optical grating couplers. Figure 11D is the cross-section of the different components of the device. The nanoresonator is etched down to 60 nm. The crystalline Si layer is highly doped locally for low metal-to-silicon contact resistance. A 200 nm amorphous silicon layer is deposited above a planarized silicon oxide layer for protection and etched open above the grating couplers and the nanoram. The AlSi is the electrical contact for the electric driving of the mechanical resonator. Light is coupled in and out of the optomechanical chips using grating couplers with a pitch of 0.6 μm and

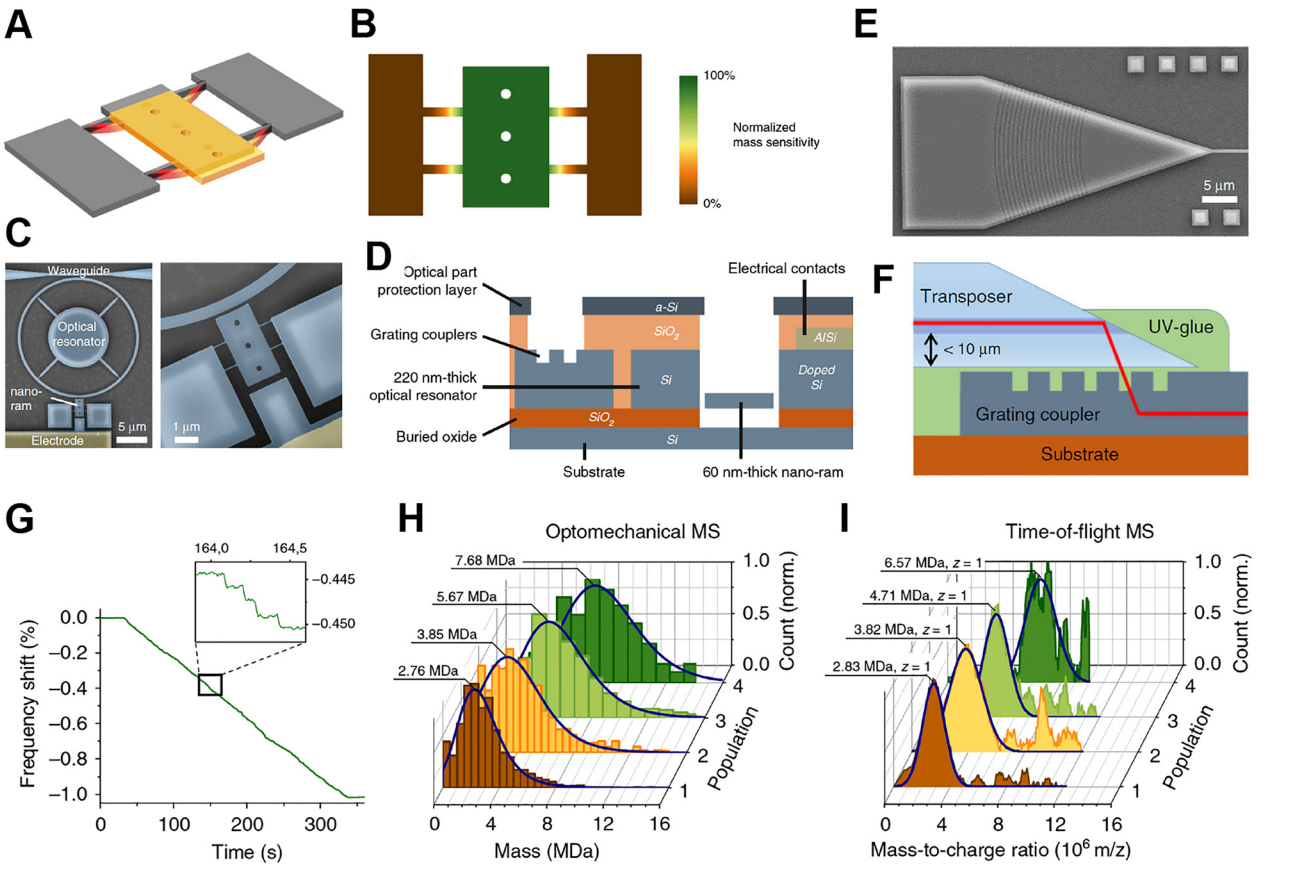

Figure 11: Single-mode optomechanical resonator for mass spectrometry [34]. (A) Mode profile of the planner mechanical resonator. (B) Mass sensitivity for different particle landing positions on the planer mechanical resonator. (C) SEM pictures of the mass spectrometer using nanomechanical resonator coupled with a microring cavity. (D) Cross section of different components of the device. (E) SEM picture of the grating structure to couple light into the microresoantor. (F) In-plane optical packaging by waveguide-to-fiber-transposer chips aligned and glued to the grating couplers. (G)–(I) Single-particle optomechanical mass spectrometry of tantalum clusters. (G) Frequency trace of the mechanical resonator for the 5.7 MDa cluster deposition. (H) Statistical distributions of different sized tantalum clusters using the optomechanical mass spectrometer. (I) Time of flight mass spectrometry for the four different tantalum clusters.

a width of 0.3 μm, designed for maximum transmission close to a 1550 nm wavelength and an input angle of 10°, as shown in Figure 11E. Figure 11F shows the quasi in-plane optical packaging by waveguide-to-fiber-transposer chips (measuring around 1 ×2× 20 mm), aligned and glued to the grating couplers.

To improve the frequency stability $\delta f/f$, therefore allowing a better mass sensitivity $\delta m_{\min} = 2M_{\text{res}}\delta f/f$, the mechanical resonator is driven electrically at its mechanical resonance f_{m}. The frequency stability is ultimately limited by intrinsic fluctuations of the resonance frequency in the mechanical domain. To reach this limit, a large SNR is required, which is maximized when the resonator is driven up to the onset of mechanical nonlinearity and when its thermomechanical noise dominates. Electrostatic actuation is performed with a side-gate 250 nm away from the nanoresonator. The frequency stability $\delta f/f$ was measured by tracking the resonance frequency of the resonator using a phase-locked-loop.

Then the mass spectrometer is demonstrated using tantalum clusters with different masses. Figure 11G–I shows single-particle optomechanical mass spectrometry of tantalum clusters. Each time a particle lands on the mechanical resonator, its resonance experiences a frequency shift, as shown in the frequency trace of the optomechanical resonator for the light green (5.7 MDa) cluster population deposition (Figure 11G). Its inset shows several frequency jumps from individual cluster depositions. Figure 11H shows the normalized nanoresonator's mass spectra for different tantalum cluster populations fitted with a log-normal function (dark blue lines) with mean masses ranging from 2.7 to 7.7 MDa (for optomechanical MS), equivalent to particle diameters from 8 to 11.3 nm. As a comparison, Figure 11I shows time of flight mass spectra for

corresponding clusters. They show good agreement, and the optomechanical mass spectrometer shows advantages for larger-sized particles.

3.3 Force sensing

The optomechanical system is capable of detecting the force exerting on the mechanical resonator with high sensitivity. According to the relation between the external force and the displacement of the resonator $F(\omega) = x(\omega)/\chi(\omega)$, the force signal can be got through the displacement detection. Therefore, the force sensitivity of the system is $\sqrt{S_{FF}(\omega)} = \sqrt{S_{xx}(\omega)}/|\chi(\omega)|$. It can be seen that the sensitivity of force detection and displacement detection only differ by a frequency-dependent response factor.

We first review the force sensors based on near-field coupling structure, which had 10 am/Hz-level sensitivity [35, 119]. In 2012, Gavartin et al. presented the integrated hybrid force detection systems. As Figure 12 shows, the hybrid structure in the vacuum chamber was composed of taper fiber, microdisk cavity, and nanomechanical beam. Gavartin et al. used three lasers with different wavelengths to provide a readout of resonator motion, feedback control, and the small incoherent radiation pressure force for direct force detection. Since the radiation pressure force was measured at room temperature, the noise that restricts the system is mainly thermal noise. Thanks to the small resonator mass (9×10^{-15} kg) and low mechanical loss (~ 38 Hz), the thermal noise of the system is $S_{FF}^{\text{th}}(\omega_m) = (74\,\text{aN})^2/\text{Hz}$. What's more, they detected a stationary incoherent force signal with a magnitude of about 1/25 of the thermal noise signal through the change of the average energy of the harmonic oscillator, demonstrating that their detecting ability was $(15\,\text{aN})^2/\text{Hz}$ [35]. It is worth mentioning that though feedback control does not better the force sensitivity [120, 121], it shortens the detection time due to the mechanical motion bandwidth improvement [122]. In 2013 Harris et al. showed that the same SNR can be achieved by properly filtering the force signal without feedback cooling. Moreover, even if there are non Gaussian or correlated noises and nonstationary processes in the system, the scheme is still applicable [120].

The force sensors utilizing the interaction between the optical cavity and the ultracold atom gas are also attractive. In 2014, shown in Figure 13, Schreppler et al. applied a calibrated optical-dipole force (Red and blue arrow) to a gas of ultracold rubidium atoms (gray ellipse), inducing center-of-mass motion of the gas. They measured the force that caused this movement in the F–P cavity. When the probe light resonated with the oscillation frequency of the cloud, the system had the best force sensitivity $\sqrt{S_{FF}} = 42 \pm 13\,\text{yN}/\sqrt{\text{Hz}}$. Since the mechanical mode of the gas was close to its base state of motion, thermal noise only accounts for a small proportion of the total noise of the system. The system was mainly limited by shot noise and backaction noise. By adjusting the system parameters, the shot noise and the backaction noise were made equal. At this time, the minimum total noise of the system could be obtained [123].

A microwave cavity-based system that works at low temperatures (~15 mK) has low thermal noise. In 2008, Regal et al. put the mechanical resonator into the cavity capacitance and achieved the sensitivity with $3\,\text{aN}/\sqrt{\text{Hz}}$ [126]. Soon after, in 2009, Teufel et al. employed a vibrating aluminum wire as a plate of the cavity capacitor, which

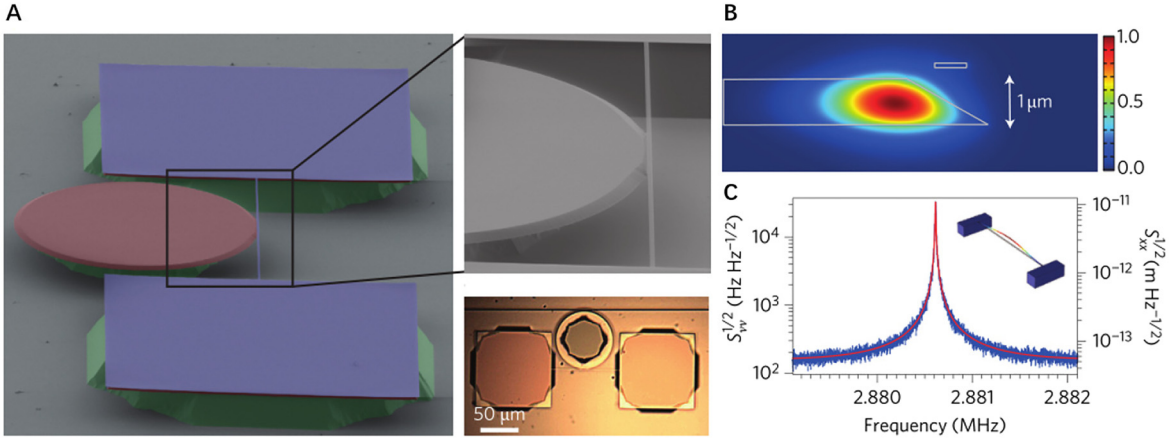

Figure 12: (A) SEM image of an integrated hybrid force detection system base on a microdisk cavity coupled with nanomechanical beam. Top right: enlarged picture of the adjacent area. Bottom right: optical micrograph of the hybrid system coupled with a tapered fiber. (B) Finite-element simulation of electric field distribution in the microdisk cavity. (C) Frequency noise units and displacement density units as a function of frequency. Finite-element simulation of the fundamental vibration mode of the beam is shown in the inset [35].

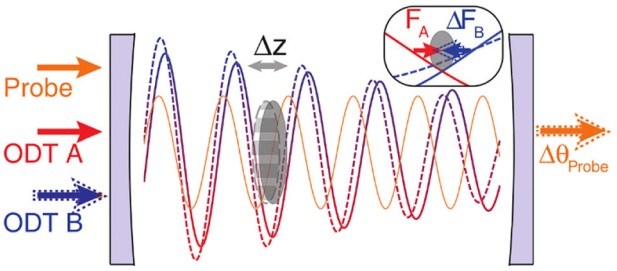

Figure 13: Schematic of gas mass center motion detection with the optomechanical system based on the F–P cavity [123].

coupled the mechanical and optical mode more naturally. Additionally, they employed a degenerate Josephson parametric amplifier to reduce the measurement technics noise and got a shot-noise-limited sensitivity of 0.51 $aN/\sqrt{Hz}$ [94]. In 2016, Weber et al. explored the performance of the multi-layer graphene mechanical vibrator coupled with the superconducting cavity system in force sensing (Figure 14) and obtained the best force sensitivity of 390 ± 30 $zN/\sqrt{Hz}$. In their system, thermal noise and the sum of shot noise and backaction noise accounted for almost 50% of the total noise.

In Table 2, we sum up some characteristic parameters of representative works in the past few years. It should be noted that since the optomechanical effects that can be exploited in each type of sensor are different, we need to select the appropriate sensor in the specific work.

Reducing the noise level of force measurement is the key to improving sensitivity. In force sensing, some work has been done to decrease quantum noise, through squeezing the state of light in injecting [127], outputting [128], measuring [129] processes, and utilizing the parametric amplifier [130, 131]. Moreover, evading backaction noise is suggested to be realized employing the F–P cavity with double movable ends [132], or coupling the cavity with a negative effective mass oscillator [127, 133]. In 2018, Mehmood et al. showed that force sensing sensitivity strongly depends upon the phase fluctuations associated with the driving laser [134]. Apart from reducing noise, there are other ways to improve sensitivity, such as enhancing signal response. In 2019, Motazedifard et al. provided a scheme that puts cigar-shaped Bose–Einstein condensate into cavities, which enhances the mechanical response of the system to the input signal [131].

Precision force detection helps improve the accuracy of atomic force microscope [36–38, 125, 135], which will be discussed in the next section in detail.

3.4 AFM and MRFM

AFM is a very high-resolution type of scanning probe microscopy, with demonstrated resolution on the order of fractions of a nanometer, more than 1000 times better than the optical diffraction limit. The AFM consists of a cantilever with a sharp tip (probe) at its end that is used to scan the specimen surface. The cantilever is typically silicon or silicon nitride with a tip radius of curvature on the order of nanometers. When the tip is brought into proximity of a sample surface, forces between the tip and the sample lead to a deflection of the cantilever according to Hooke's law. The deflection of cantilever is usually readout by shining a light beam onto the cantilever, and measuring the phase change of the light. Several different aspects of the cantilever motion can be used to quantify the interaction between the tip and sample, including the value

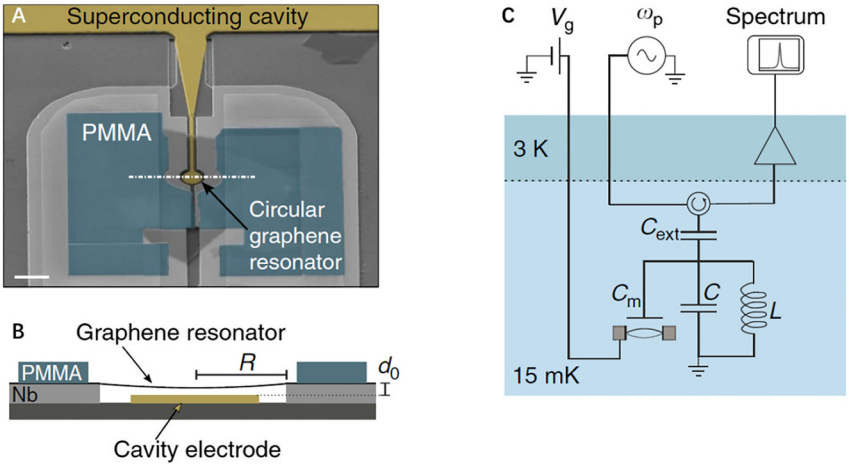

Figure 14: (A) False-color image of multilayer graphene optomechanical devices. (B) Cross-sectional illustration of the graphene resonator along the white dashed dotted line in (A). (C) Schematic of the detection circuit. The superconducting cavity couples with the graphene mechanical resonator through the capacitance [124].

Table 2: Summary of sensitivities for force sensing experiments in optomechanical systems.

Device type	$\sqrt{S_{FF}}(N/\sqrt{Hz})$	m_{eff} (kg)	Q_m	G (MHz · nm^{-1})	Year
1. Microdisk cavity-nanobeam [35]	1.5×10^{-17}	9.0×10^{-15}	4.8×10^{5}	1.8×10^{1}	2012
2. Microdisk cavity-ring [119]	5.3×10^{-17}	–	1.4×10^{3}	1.3×10^{4}	2012
3. Microdisk cavity-cantilever [125]	1.3×10^{-16}	6.1×10^{-16}	7.8×10^{3}	7.0×10^{0}	2014
4. F–P cavity-rubidium atoms [123]	4.2×10^{-23}	1.8×10^{-22}	3.7×10^{1}	1.3×10^{2}	2014
5. Microwave cavity - nanowire [126]	3.0×10^{-18}	2.0×10^{-15}	2.3×10^{3}	7.3×10^{3}	2008
6. Microwave cavity-nanowire [94]	5.1×10^{-19}	1.1×10^{-14}	$(0.5 \sim 1.5) \times 10^{2}$	2.1×10^{-1}	2009
7. Microwave cavity-nanowire [124]	3.9×10^{-19}	9.6×10^{-18}	2.0×10^{5}	3.3×10^{-1}	2016
8. F–P cavity-membrane [103]	1.1×10^{-17}	2.3×10^{-12}	1.0×10^{9}	4.2×10^{-1}	2019

of the deflection, the amplitude of an imposed oscillation of the cantilever, or the shift in resonance frequency of the cantilever. To make the phase change of light measurable, the cantilevers are usually made to be comparable to the light spot size, which is usually at micrometer scale. Reducing the cantilever size to nanoscale dimensions can improve the bandwidth and sensitivity, but current optical transduction methods suffer when the cantilever is small compared to the achievable spot size.

In recent years, researchers have developed cavity optomechanical systems for AFM applications, in which the mechanical resonator works as the cantilever probe whose mechanical oscillation can be sensitively readout using an optical microcavity, providing high sensitivity and bandwidth. In reference [36], Srinivasan et al. demonstrated sensitive optical transduction in a monolithic cavity optomechanical system in which a subpicogram nanoscale silicon cantilever with a sharp probe tip is separated from a microdisk optical resonator by a nanoscale gap (Figure 15A). The nanoscale cantilever has resonance frequencies of tens of MHz and their thermally driven vibrations can be transduced by the microdisk optical modes with high quality factor (around 10^5). The displacement sensitivity has reached to 4.4×10^{-16} m/$\sqrt{\text{Hz}}$, the bandwidth is larger than 1 GHz, and the dynamic range is estimated to be larger than 10^6 for a 1-s measurement.

Later in 2017, Chae et al. used this nanocantilever-microdisk coupled system to realize functional AFM detection with high temporal resolution (10 ns) and picometer vertical displacement uncertainty simultaneously [37]. With the ability to capture fast events with high precision, this work realized the measurement of the thermal conductivity for the first time, concurrently with chemical composition at the nanoscale in photothermal induced resonance experiments (Figure 15B). The paradigm-shifting photonic readout for small probes breaks the common trade-off between AFM measurement precision and ability to capture transient events, thus transforming the

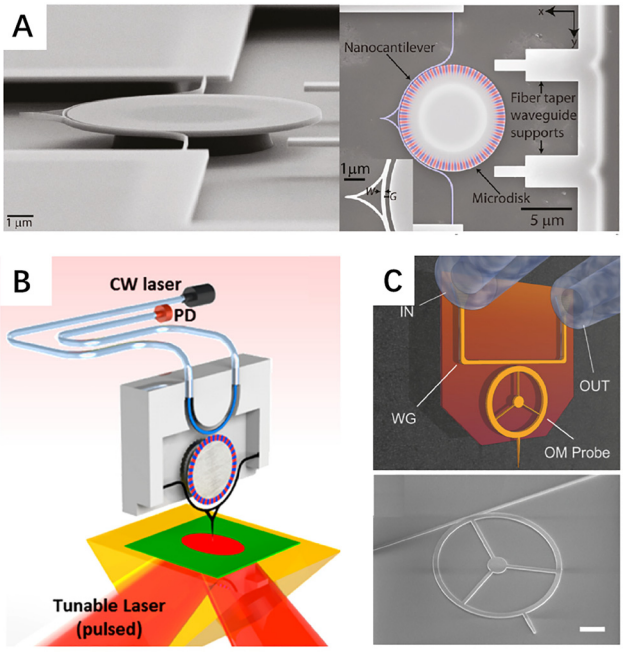

Figure 15: Atomic force microscope using cavity optomechanical systems. (A) Integrated silicon microcatileter probe which is optomechanically transduced using a microdisk [36], (B) photonic transducer photothermal induced resonance: a fiber-pigtailed, integrated transducer leverages cavity optomechanics to measure motion of a nanoscale probe, radically reducing the noise and increasing the measurement bandwidth for capturing the sample's fast thermalization dynamics induced by laser pulses [37]. (C) Top: optomechanical probe with resonance frequency larger than 100 MHz, which couples light through a waveguide (WG) and two fiber grating couplers (IN and OUT). Bottom: SEM micrograph of the optomechanical probe, used in [38].

ability to observe nanoscale dynamics in materials. In 2020, Allain et al. introduced a resonating optomechanical atomic force probe at a frequency of 117 MHz, two orders of magnitude above traditional AFM cantilevers, with a Brownian motion amplitude four orders below (Figure 15C) [38]. Using this technology, they demonstrated both

contact and noncontact AFM, which can measure interactions with subpicometer amplitude with very fast speed.

By functionalizing AFM, more measurements can be performed. For example, magnetic force microscopy (MFM) uses a sharp magnetized tip to scan a magnetic sample, and the tip-sample magnetic interactions are detected and used to reconstruct the magnetic structure of the sample surface. The MRFM concept combines the ideas of magnetic resonance imaging (MRI) and AFM. MRFM uses a cantilever tipped with a ferromagnetic (iron cobalt) particle to directly detect a modulated spin gradient force between sample spins and the tip. MRI is well known as a powerful technique for visualizing subsurface structures with three-dimensional spatial resolution. Pushing the resolution below 1 mm remains a major challenge, however, owing to the sensitivity limitations of conventional inductive detection techniques. Currently, the smallest volume elements in an image must contain at least 10^{12} nuclear spins for MRI-based microscopy, or 10^7 electron spins for electron spin resonance microscopy. MRFM was then proposed as a means to improve detection sensitivity to the single-spin level, and thus enable three-dimensional imaging of macromolecules (for example, proteins) with atomic resolution. The magnetic particle is characterized using the technique of cantilever magnetometry. As the ferromagnetic tip moves close to the sample, the atoms' nuclear spins become attracted to it and generate a small force on the cantilever. The spins are then repeatedly flipped, causing the cantilever to gently sway back and forth in a synchronous motion. That displacement is measured with a laser beam interferometer to create a series of two-dimensional images of the sample, which are combined to generate a three-dimensional image. The interferometer measures the resonant frequency of the cantilever. Using smaller ferromagnetic particles and softer cantilevers can increase the SNR.

In 2003, Mamin et al. developed an MRFM based on an ultrasensitive cantilever mounted perpendicular to the sample [39]. At the end of the cantilever is a micron-size SmCo magnetic particle that generates a strong magnetic field gradient. A microwave field from a superconducting resonator is applied to excite electron spin resonance. The inhomogeneity of the tip field confines the magnetic resonance to the region that satisfies the condition $B_0 = \omega_{mw}/\gamma_g$, where ω_{mw} is the frequency of the microwave field, γ_g is the gyromagnetic ratio, and B_0 is the tip field (Figure 16A). Using this MRFM, they report the detection of the $\sqrt{N}$ statistical polarization in a small ensemble of electron spin centers in silica by MRFM. Using field gradients as high as 5 G/nm, they achieved a detection sensitivity equivalent to roughly two electron spins, and observed spin-lock lifetimes as long as 20 s. In 2004, Rugar et al. reported the detection of an individual electron spin by MRFM [40], using a very similar MRFM system (Figure 16B), with an interrupted oscillating cantilever-driven adiabatic reversal (iOSCAR) protocol. The cyclic spin inversion causes a slight shift of the cantilever frequency owing to the magnetic force exerted by the spin on the tip. A spatial resolution of 25 nm in one dimension was obtained for an unpaired spin in silicon dioxide. Spins as deep as 100 nm below the sample surface can be probed.

In 2019, Fischer et al. developed an MRFM using a high-stress silicon nitride membrane mechanical resonator [41] to image spins at room temperature. They use a "trampoline" membrane resonator with a quality factor above 10^6. A Michelson interferometer is used to readout the trampoline mechanical resonator. With this system, they demonstrated electron spin resonance of an ensemble of electron spins in diphenylpicrylhydrazil (DPPH) at room temperature using the trampoline resonators functionalized with a magnetic grain (Figure 16C). Such high-stress resonators can potentially reach 0.1 aN/$\sqrt{\text{Hz}}$ force sensitivities at MHz frequencies by using techniques such as soft clamping and phononic-crystal control of acoustic radiation in combination with cryogenic cooling. This MRFM could also be combined with an integrated F–P cavity

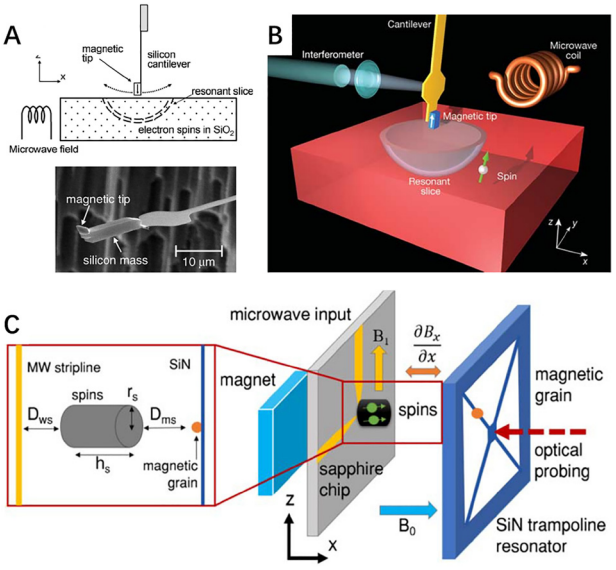

Figure 16: Magnetic force microscope using cavity optomechanical systems [39–41]. (A) Ultrasensitive silicon cantilever coated with a microsize SmCo magnetic particle at the end is used as an MRFM probe, to detect the electronic spins in silica [39]. (B) Configuration of the single-spin MRFM experiment [40]. (C) Experimental schematic for magnetic resonance force microscopy using a silicon nitride membrane mechanical resonator [41].

readout at cryogenic temperatures, to further increase the sensitivity.

3.5 Acceleration sensing

Acceleration sensing is essential for various applications ranging from inertial navigation to consumer electronics. Typical acceleration sensing is performed by measuring the displacement of a flexibly mounted test mass sensitively, which can be realized using capacitive, piezoelectric, tunnel-current, or optical methods. Optical detection provides superior displacement sensitivity, resilience to electromagnetic interference and long-range readout. Cavity optomechanical systems with ultrahigh displacement sensitivity provide an ideal platform for on-chip, high sensitivity, and broad bandwidth accelerometers. In 2012, Krause et al. demonstrated an optomechanical accelerometer that made use of ultrasensitive displacement readout using a photonic crystal zipper nanocavity monolithically integrated with a nanotethered test mass of high mechanical Q factor. The device achieved an acceleration sensitivity of 10 ng/$\sqrt{\text{Hz}}$ with submilliwatt optical power, a bandwidth of more than 20 kHz, and a dynamic range of greater than 40 dB [42].

Figure 17A shows the basic principle of operation of an accelerometer. When subjected to an acceleration a, a mechanically compliant test mass experiences a displacement $x(\omega) = m_{\text{eff}} a(\omega)\chi(\omega)$, in which $\chi(\omega)$ is the mechanical susceptibility. Figure 17B shows the displacement in response to the acceleration. It shows a peak on the mechanical resonance frequency, suggesting that having a high Q mechanical test mass is important for high sensitivity accelerometer. Figure 17C shows the false-colored SEM image of the optomechanical accelerometer, consisting of a photonic crystal zipper cavities with one of the zipper cavity connected to a nanotethered test mass. A test mass with dimensions of 150 μm × 60 μm × 400 nm (green) is suspended on highly-stressed 150-nm wide and 560-μm long nanotethers, which allow for high mechanical frequencies (27 kHz) and high mechanical quality factors (10^6). On the upper edge of the test mass, a zipper photonic crystal nanocavity (pink) is implemented. The zoom-in view of the photonic crystal zipper cavity is shown in Figure 17D, showing its electric field distribution of the fundamental bounded mode of the zipper cavity. When the test mass experiences a displacement due to external acceleration, the gap between the two coupled photonic crystal nanocavities changes (Figure 17E), therefore shifting the optical resonance of the zipper cavity mode. Figure 17F shows the SEM picture of an array of devices with different test masses.

A dimpled tapered fiber is used to couple light into the zipper cavity to optically read out the mechanical motion of the test mass. A balanced photodetector is used to measure the photocurrent out of the tapered fiber. The optically detected noise power spectrum is shown in the left axis of Figure 17G, showing a mechanical resonance at around 27.5 kHz. The equivalent displacement noise power spectrum is shown on the right axis. The tone at 26 kHz (orange) is the transduction of a tone applied to the shear piezo corresponding to an acceleration of 38.9 mg. The dashed and dotted lines are theoretical noise levels for shot noise (red), detector noise (cyan), thermal noise (green), and the total of all noise contributions (purple). The response of the sensor as a function of frequency is measured by scanning the frequency of acceleration applied to the sensor. Calibrated from the noise power spectrum and the response spectrum, the sensitivity NEA is derived, as shown in Figure 17H, showing a broad bandwidth of tens of kHz. The dashed red line depicts the theoretical expectation for the NEA given shot noise and thermal noise limitations. The green dashed curve corresponds to the thermal noise (a_{th}).

Later in 2014, Cervantes et al. from NIST developed another cavity optomechanical accelerometer, consisting of a F–P fiber optic microcavity with one end of the fiber cavity connected to a silica mechanical resonator [43]. With a displacement sensitivity of 200 am/$\sqrt{\text{Hz}}$ of the test mass, this F–P fiber optic microcavity optomechanical accelerometer has achieved an excellent acceleration sensitivity. At lower frequencies of 10–100 Hz, it has reached a comparable resolution to conventional devices at μg/$\sqrt{\text{Hz}}$ levels and improving to sub μg/$\sqrt{\text{Hz}}$ through 1 kHz. Unprecedented sensitivities below 100 ng/$\sqrt{\text{Hz}}$ over 10 kHz are achieved above 1.5 kHz, and better than 10 ng/$\sqrt{\text{Hz}}$ slightly above 9 kHz over approximately 2 kHz.

3.6 Magnetic field sensing

Ultrasensitive magnetic field sensing has various important applications, such as magnetic anomaly detection [136], mineral exploration [137], MRI [138, 139], and magnetoencephalography (MEG) [140, 141]. Currently, the most technologically advanced magnetometer is based on the superconducting quantum interference device (SQUID) [142, 143]. However, the requirement of cryogenic cooling increases the complexity of SQUID magnetometers. To circumvent this requirement, various high precision magnetometers without the cryogenic environment have been developed in the last few decades, such as atomic magnetometers [144, 145], nitrogen-vacancy center magnetometers [146, 147], and cavity optomechanical magnetometers [44–53]. Among them, cavity optomechanical

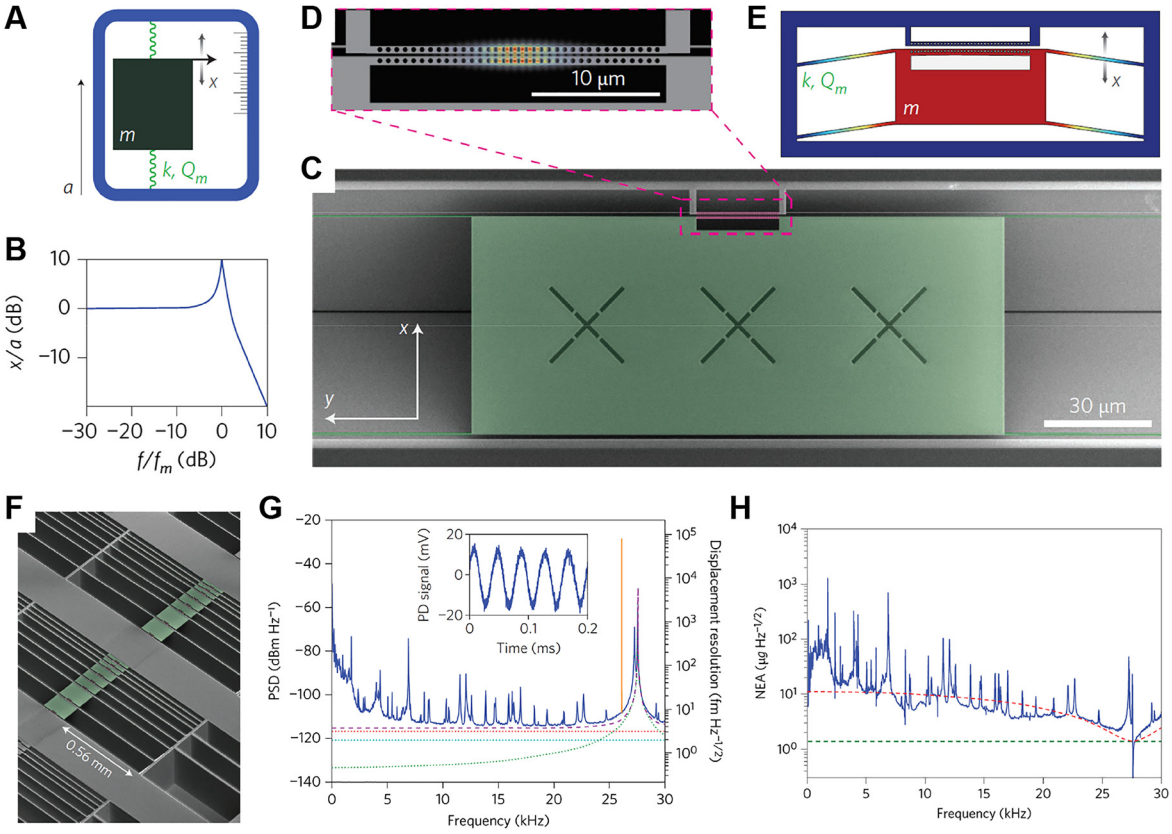

Figure 17: An on-chip optomechanical accelerometer [42]. (A) Canonical example of an accelerometer. When the device experiences a constant acceleration a, a test mass m undergoes a displacement $x = ma/k$, in which k is the spring constant of the mechanical resonator. (B) Frequency response $\chi(\omega)$ of an accelerometer in an log–log plot, showing a mechanical resonance at frequency $f_m = \sqrt{k/m}/2\pi$ with mechanical quality factor $Q_m = 10$. (C) False-colored SEM image of the optomechancial accelerometer. (D) Zoom in of the zipper photonic crystal nanocavity, showing the electric field $|E(r)|$ of the fundamental bounded mode of the zipper cavity. The top beam is mechnically anchored to the bulk SiN and the bottom beam is attached to the test mass. (E) Schematic displacement profile of the fundamental in-plane mechanical mode used for acceleration sensing. (F) SEM image of an array of devices with different test mass sizes. (G) Left axis: optical power spectral density of the balanced photodetector signal showing mechanical modes at 27.5 kHz. Right axis: equivalent displacement noise. The tone at 26 kHz is transduction of the acceleration signal applied to the shear piezo corresponding to an acceleration of 38.9 mg. The dashed and dotted lines are theoretical noise levels for shot noise (red), detector noise (cyan), thermal noise (green), and the total noise (purple). Inset: time trace of the transduction of an applied acceleration of 35.6 mg at 25 kHz. (H) Frequency-dependent noise equivalent acceleration (NEA) of the device, quantifying its broadband resolution.

magnetometers offer the advantages of small size, weight, and power consumption; ease of on-chip integration; high sensitivity; and broad bandwidth. The presence of mechanical and optical resonances greatly enhances both the response to the magnetic field and the measurement sensitivity. In the last decade, a lot of efforts have been made to achieve on-chip, high-sensitivity cavity optomechanical magnetometers.

Cavity magnetometry was first developed in 2012 by Forstner et al. [44]. The idea was to combine magnetostrictive material into a high Q_o microtoroid cavity. The expansion of the magnetostrictive material is resonantly transduced into the physical structures of a highly compliant microresonator and optically readout out with high sensitivity. As the first proof of principle demonstration of a cavity optomechanical magnetometer, a piece of Terfenol-D with a size of a few tens of microns was affixed to the top surface of a microtoroid by using micromanipulators and two-component epoxy. A probe laser is locked on the side of an optical resonance, and the mechanical motion of the microcavity translates into a periodic modulation of the intracavity power and is detected with a spectrum analyzer. The magnetic response of the magnetometer is measured by a network analyzer when the frequency of the driving magnetic field is swept. A peak sensitivity of 400 $\mathrm{nT}/\sqrt{\mathrm{Hz}}$ was achieved, with theoretical modeling predicting the possibility of sensitivities below 1 $\mathrm{pT}/\sqrt{\mathrm{Hz}}$ using this cavity optomechanical magnetometer.

The sensitivity and bandwidth of the first demonstrated cavity optomechanical magnetometer were critically constrained by the poor coupling of the magnetostrictive expansion to the mechanical resonance of the device, because that the expansion of the magnetostrictive material and the mechanical motion are not on the same plane. In order to overcome this problem, Forsterner et al. later in 2014 developed a new device structure with the magnetostrictive material embedded directly within the microtoroid. The magnetic field sensitivity was significantly improved by three orders of magnitude, with a peak sensitivity at a level of 200 $\mathrm{pT}/\sqrt{\mathrm{Hz}}$, and a bandwidth of around 40 MHz [45]. In addition, by employing the nonlinearities inherent in the magnetostrictive material, low frequency magnetic field response can be mixed up to the high frequency range, and therefore can be indirectly measured. Magnetic field sensing with frequencies as low as 2 Hz has also been realized, with a sensitivity of 150 $\mathrm{nT}/\sqrt{\mathrm{Hz}}$ [45]. In 2020, Li et al. has further improved the sensitivity of the microtoroid based magnetometer to a level of 26 $\mathrm{pT}/\sqrt{\mathrm{Hz}}$ and the bandwidth to 130 MHz [49], by optimizing the geometrical structure of the magnetometers (Figure 18A).

The above-mentioned fabrication method by manually epoxy bonding a grain of magnetostrictive material has several challenges. First, the manual deposition process requires the precise positioning of microsized grains relative to the microcavity. Second, the use of epoxy bonding makes the approach ill-suited for scalable fabrication. Furthermore, both optimization of the overlap of the magnetostriction to mechanical motion and reproducible performance across devices are hard to realize due to the random geometry, orientation, and size of the magnetostrictive material grain in each device. To overcome these challenges, in 2018, Li et al. developed a controllable fabrication method, which involves deterministically sputter coating thin films onto the microcavities (Figure 18B) [47]. These sputter-coated magnetometers got relatively good reproducibility across devices, and a peak sensitivity of 585 $\mathrm{pT}/\sqrt{\mathrm{Hz}}$ is achieved. They also showed that thermally annealing of the sputtered film can improve the magnetometer sensitivity by a factor of 6.3.

The microtoroids have mechanical resonances in the ranges of MHz to tens of MHz, and therefore the magnetometers based on microtoroid cavities have good sensitivity in the MHz frequency range, which is suitable for

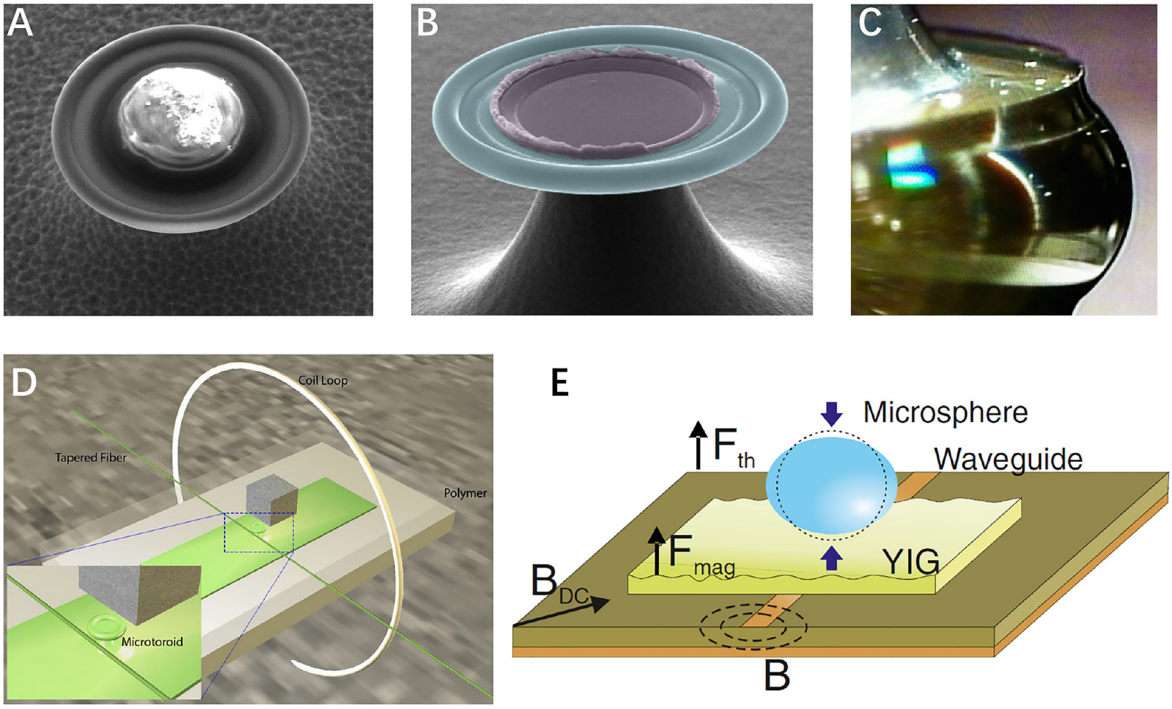

Figure 18: Cavity optomechanical magnetometers. (A) Cavity optomechancial magnetometry using microtoroids with particles of magnetostrictive material Terfenol-D embedded inside [49]. (B) Cavity optomechanical magnetometry using microtoroids with a thin film of Terfenol-D sputter coated inside [47]. (C) Cavity optomechanical magnetometry using a cm-size CaF_2 resonator with a cylinder of Terfenol-D embedded inside [46]. (D) A magnetometer using a microtoroid with a microsized magnet embedded inside the cavity, capsulated using poly(dimethylsiloxane) (PDMS) [50]. (E) Magnetometry working at hundreds of MHz to a few GHz, assisted by ferromagnetic resonance in a yttrium iron garnet (YIG) film, whose mechanical motion is read out through a microsphere [52].

applications such as MRI. Other applications, such as magnetic anomaly detection and MEG, need high magnetic field sensitivity at low frequencies (Hz to kHz range). One straightforward idea is to increase the size of the cavity and thus to decrease the mechanical resonance frequencies. In 2016, Yu et al. demonstrated a centimeter-scale optomechanical magnetometer using a crystalline CaF_2 whispering gallery mode resonator with a cylinder of Terfenol-D embedded inside (Figure 18C). The large size of the resonator, with a magnetic field integration volume of 0.45 cm^3, allows high magnetic field sensitivity to be achieved in the hertz-to-kilohertz frequency range. A peak sensitivity of 131 $pT/\sqrt{Hz}$ was achieved, in a magnetically unshielded noncryogenic environment [46]. Femtotesla range sensitivity may be possible in future devices with the further optimization of laser noise and the physical structure of the resonator. Another work that achieved good magnetic field sensitivity at a low frequency range was done by Zhu et al. in 2017. They demonstrated a magnetometer using polymer encapsulated whispering gallery mode microcavity actuated by a micro-magnet (Figure 18D). The magnetic field induces a force on the micro-magnet causing deformation in the polymer around the cavity. The deformation induces a refractive index change in the polymer which can be optically readout through the transmitted light from the cavity. Due to the relatively large size of the magnetometer and thus low mechanical resonances, this magnetometer works at hertz-to-kilohertz range and achieved a sensitivity of 880 $pT/\sqrt{Hz}$ [50]. Polymer encapsulation and fiber optical connection ensure the environmental robustness and practicality of the sensor. In another work, by elastically coupling a magnet to a sphere shell cavity, a sensitivity of 60 $nT/\sqrt{Hz}$ at 100 Hz has been realized [51].

Except for the efforts made in low-frequency cavity optomechanical magnetometry, researchers have also developed magnetometers that work at high-frequency ranges (from hundreds of MHz to GHz). In 2020, Colombano et al. demonstrated a hybrid magnetometer that exploits the coupling between the resonant excitation of spin waves in a ferromagnetic insulator and the resonant excitation of the breathing mechanical modes of a glass microsphere deposited on top. The interaction is mediated by magnetostriction in the ferromagnetic material and the consequent mechanical driving of the microsphere. The magnetometer response thus relies on the overlap between the ferromagnetic resonance and the mechanical modes of the sphere, leading to a peak sensitivity of 850 $pT/\sqrt{Hz}$ at 206 MHz. By externally tuning the ferromagnetic resonance using an external static magnetic field, a sensitivity on the ferromagnetic resonance of a few $nT/\sqrt{Hz}$ is achieved at GHz frequency range, providing a platform for high-speed magnetic field sensors.

Another type of cavity optomechanical magnetometer is torque magnetometry. A torque magnetometer can either detect the magnetic moment $\vec{m}$ of a magnetic material or an external magnetic field $\vec{B}$, by measuring the torque $\vec{\tau} = \vec{m} \times \vec{B}$ exerted on the magnetic material by an external magnetic field $\vec{B}$. A torque magnetometer can be realized by depositing a magnetic material onto a cantilever [148, 149] or a torsional [150–155] mechanical resonator. For instance, torsional torque magnetometers have been realized by focused-ion-beam milling of permalloy coated silicon nitride membranes and reading out the torsional mechanical response using optical interferometry. By varying the bias magnetic field, the magnetic behavior with an excellent sensitivity around $10^8 \mu_B$ for sing magnetic element [150]. These torsional torque magnetometers have been used to measure the magnetic hysteresis in microscale permalloy [151], magnetic supercooling of the transition to the vortex state [152, 156], and the Barkhausen effect in magnetic materials [153]. AC susceptometry [154] and Torque-mixing magnetic resonance spectroscopy [155] have also been realized using these torsional torque magnetometers.

Combining optical cavities with the torque magnetometers can further improve the sensitivity, due to the optical resonance enhanced transduction. In 2003, Kim et al. fabricated a nanoscale torsional resonator evanescently coupled to optical microdisk whispering gallery mode resonators [157]. The on-chip, integrated devices are measured using a fully fiber-based system. With a thermomechanically calibrated optomechanical noise floor down to 7 $fm/\sqrt{Hz}$, these devices open the door for a wide range of physical measurements involving extremely small torques, as little as 4×10^{-20} Nm. By cooling the system to a temperature of 25 mK, the torque sensitivity can be improved to 2.9×10^{-24} Nm [71]. Magnetic actuation and feedback cooling have been realized using this torque-cavity system [85]. Broadband optomechanical transduction of nanomagnetic spin mode in a permalloy disk was also realized [158].

In addition, optomechanical transduction of a torque magnetometer using photonic crystal nanobeam cavities has also been demonstrated [53, 74]. In 2014, Wu et al. demonstrated a phototonic crystal split-beam nanocavity for detecting the nanoscale source of torque. Both dissipative and dispersive couplings are experimentally observed, with a dissipative coupling of up to approximately 500 MHz/nm and dispersive coupling of 2 GHz/nm. This enables the measurement of sub-pg torsional and

cantilever-like mechanical resonances with a thermally limited torque detection sensitivity of 1.2×10^{-20} Nm/$\sqrt{\text{Hz}}$ in ambient conditions and 1.3×10^{-21} Nm/$\sqrt{\text{Hz}}$ in low vacuum [74]. Further, they demonstrated the potential of this nanophotonic optomechanical system as a torque magnetometer and radiofrequency magnetic susceptometer [53]. The structure of the optomechanical system is shown in the SEM picture in Figure 19A, in which a split photonic crystal nanocavity is integrated within a torsional nanomechanical resonator. At the end of one split nanocavity is coated with a 40 nm thick permalloy island. The field distribution of its optical resonance is shown in the bottom panel of Figure 19A. The exquisite readout sensitivity enables observations of the unique net magnetization and RF-driven responses of single mesoscopic magnetic structures in ambient conditions. The magnetic moment resolution is sufficient for the observation of Barkhausen steps in the magnetic hysteresis of a lithographically patterned permalloy island (Figure 19B and C).

3.7 Ultrasound sensing

Ultrasound sensing has various important applications in biomedical imaging, photoacoustic sensing, and non-destructive industrial monitoring. Currently, piezoelectric transducers represent state-of-the-art ultrasound sensors, but have some limitations. First, achieving high sensitivity usually needs millimeter to centimeter sized piezoelectric elements. However, this results in a highly directional response to MHz frequency due to spatial averaging, which can degrade image signal to noise ratio for applications that require omnidirectional response such as photoacoustic imaging. Second, achieving the highest sensitivity usually requires detectors that are fabricated from acoustically resonant piezoceramic materials. This can result in a sharply peaked frequency response thereby precluding a faithful representation of the incident acoustic wave and ultimately compromising image fidelity. Optical ultrasound sensors, offer an alternative, and are beginning to challenge the current piezo-electric dominated landscape, especially those based on highly sensitive optically resonant structures such as microtoroids, microspheres microdisks, microrings, F–P interferometers, and in-fiber Bragg gratings. These microresonators detect acoustic waves through photoelastic effect or acoustic pressure induced deformation of the microresonators, both of which can be optically read out. These ultrasound sensors have several advantages in terms of ultrasound sensing performances. First, ultrasound sensors based on optical microresonators provide high sensitivity, due to the optical resonance enhanced interaction length, which usually can reach thermal noise or shot noise limited level, instead of electronic noise limited regime in the piezoelectric case. Second, they have low directivity at MHz frequencies, due to the microscale sizes. In addition, microresonators can be scalably fabricated on a chip, and therefore provide the

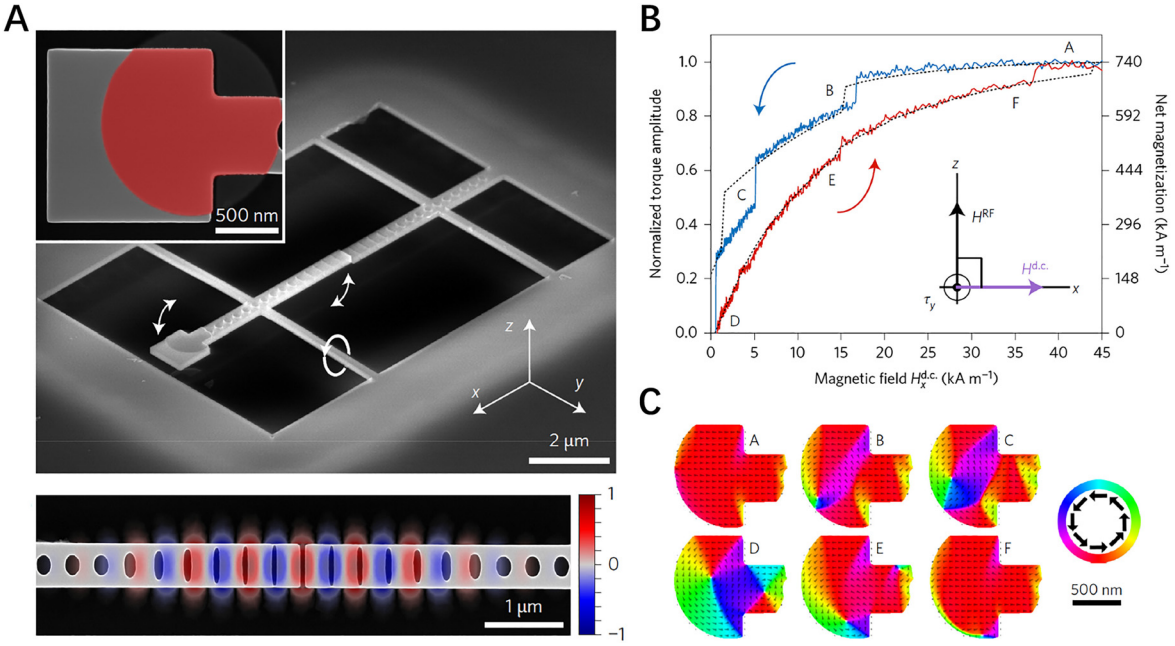

Figure 19: (A) A torque magnetometer using split photonic crystal nanobeams with a micro-sized magnetic material deposited on one of the beams [53]. (B)–(C) Barkhausen steps in the magnetic hysteresis of a lithographically patterend permalloy island, measured using the torque magnetometer.

possibility of multichannel detectors for imaging with high spatial resolution.

Silica microresonators with different geometries have been used for ultrasound sensing, due to their high Q_0 factor. In 2013, Monifi et al. demonstrated ultrasound sensing using a microtoroid together with its side coupled tapered fiber encapsulated in a low refractive index polymer, through detecting the optical transmission change induced by ultrasound. The achieved optical Q_0 factor is 6×10^6, and a response of 35 mV/kPa [54]. In 2014, Chistiakova et al. used an ultra-high Q_0 silica microsphere (Figure 20A) to detect ultrasound at 12 MHz, and has achieved an ultra-high ultrasound response 4911 mV/kPa of and a low noise equivalent pressure (NEP) of 0.535 Pa [55]. In 2017, Kim et al. demonstrated ultrasound sensing in an air environment using a high Q_0 ($\sim 10^7$) silica capillary microresonator (Figure 20B), and achieved an NEP of 215 mPa/$\sqrt{\text{Hz}}$ and 41 mPa/$\sqrt{\text{Hz}}$ at 50 and 800 kHz, respectively [56]. In 2020, Pan et al. presented ultrasound sensing based on a digital optical frequency comb (DOFC) technique combined with high-Q_0 optical microbubble resonators. DOFC enables precise spectroscopy on resonators that can trace the ultrasound pressure with its resonant frequency shift with femtometer resolution and sub-microsecond response time. This system enables precise spectroscopy on resonators that can trace the ultrasound pressure with its resonant frequency shift with femtometer resolution and sub-microsecond response time. The achieved NEP of air-coupled ultrasound is 4.4 mPa/$\sqrt{\text{Hz}}$ by combining a high Q_0 ($\sim 3 \times 10^7$) microbubble resonator with the DOFC method [58].

In addition to using optical resonance enhanced readout sensitivity, exploring mechanical resonance in microresonators can also increase its response to an external ultrasound, therefore increasing the sensitivity. In 2019, Sahar et al. has achieved ultrasensitive ultrasound sensing using a lithographically fabricated microdisk suspended above a silicon chip via thin tethers (Figure 20C). By engineering its structure for high-acoustic sensitivity, for the first time, they have reached a regime where gas molecule collisions dominate the noise floor. This allows NEP of 8–300 μPa/$\sqrt{\text{Hz}}$ in the frequency range between 1 kHz and 1 MHz [57]. Compared to acoustic sensors that use similar, but nonsuspended, optical cavities and rely on refractive index shifts and static deformations rather than nanomechanical resonances, the peak sensitivity represents a more than three order-of-magnitude advance. Normalized by device area, it outperforms all previous air-coupled ultrasound sensors by two orders of magnitude at ultrasound frequencies from 80 kHz to 1 MHz. In 2020, Yang et al. demonstrated an optomechanical microdevice based on Brillouin lasing in an optical microcavity to sense external light, sound, and microwave signals, through the modulations to the microcavity Brillouin laser

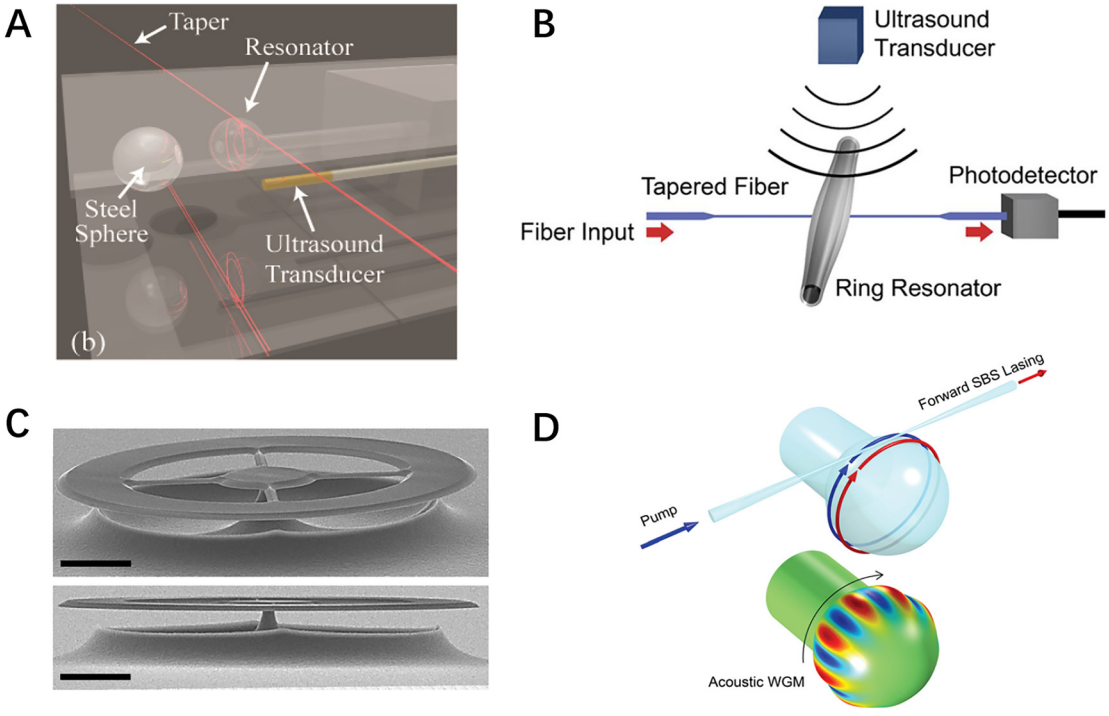

Figure 20: Acoustic sensing using different cavity optomechanical systems: (A) silica microsphere cavity [55], (B) silica microbottle cavity [56], (C) silica microdisk cavity [57], and (D) stimulated Brillioun lasing in silica microspheres [63].

in a resonance-enhanced manner through either pressure forces including radiation pressure force or thermal absorption (Figure 20D). They achieved an acoustic sensing NEP of 267 μPa/$\sqrt{\text{Hz}}$ at the kHz frequency range [63].

In order to achieve high ultrasound sensitivity at tens of MHz frequency, Guggenheim et al. demonstrated a plano-concave polymer F–P microresonator for high sensitivity and broadband acoustic sensing, as shown in Figure 21. The sensor comprises a solid plano-concave polymer microcavity formed between two highly reflective mirrors (Figure 21A). The cavity is embedded within an encapsulating layer of identical polymer so as to create an acoustically homogeneous planar structure. The cavity itself is constructed by depositing a droplet of optically clear UV-curable liquid polymer onto a dielectric mirror coated polymer substrate. The droplet stabilizes to form a smooth spherical cap under surface tension and is subsequently cured under UV light. The second dielectric mirror coating is then applied, followed by the addition and curing of further polymer to create the encapsulating layer. Laser light is incident from the bottom of the cavity, and is used to measure the acoustic wave induced deformation of the cavity. This plano-concave microresonator has achieved a strong optical confinement with a Q_0 factor 10^5, resulting in a high sensitivity of 1.6 mPa/$\sqrt{\text{Hz}}$, and a broad bandwidth up to 40 MHz [59]. One distinguishing feature of this plano-concave microresonator is that it can be integrated at the end of a fiber, and therefore be used as a fiber probe for photoacoustic imaging applications (Figure 21B). They used this microresonator on a fiber system to demonstrated optical-resolution photoacoustic imaging of mouse ear vasculature *in vivo* (Figure 21C).

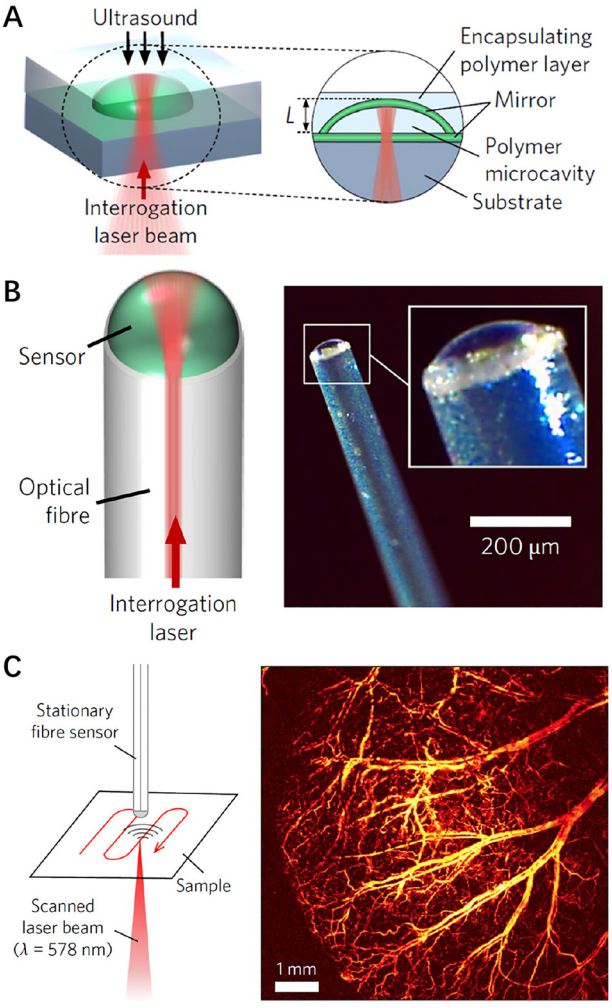

Figure 21: Acoustic sensing using a plano-concave F–P -cavity [59]. (A) Schematic of the plano-concave polymer microresonator. (B) Microresonator fabricated at the end of the fiber for imaging applications. (C) Photoacoustic imaging demonstrated using this plano-concave polymer microresonator.

Integrated microresonators can be massively fabricated on a chip, and therefore provide an ideal platform for high-resolution photoacoustic imaging applications. Polymer materials are generally much softer than dielectric materials, and therefore can be easily deformed by ultrasound, producing large sensing signals. In addition, polymer materials can be easily fabricated into microresonators through the nanoimprinting method, allowing for acquiring volumetric photoacoustic images with cellular/subcellular resolution in three dimensions. In 2014, Zhang et al. demonstrated an ultrasonic detector with unprecedented broad bandwidth and high sensitivity, based on an imprinted polymer optical microring (Figure 22A). The polymer microring was fabricated by nanoimprinting of polystyrene (PS) film using a silicon mold. The imprinting process simplifies fabrication, increases throughput, and improves reproducibility. The device consists of a ring resonator (with Q_0 factor of 1.3×10^5) coupled with a bus waveguide. It has an acoustic response of up to 350 MHz at −3 dB and noise-limited detectable pressure as low as 105 Pa in this frequency range [60]. In 2014, Li et al. demonstrated photoacoustic sensing using an SU8 polymer microring resonator nanofabricated on a 250 μm thickness microscope coverslip (with Q_0 factor of 10^4), with a bandwidth of 140 MHz and an NEP of 6.8 Pa [61]. In 2019, the same group reported a disposable ultrasound sensing chronic cranial window using an integrated PDMS microring fabricated using a soft nanoimprint lithography process (Figure 22B). The device was surgically implanted on the skull to create a self-contained environment, maintaining optical access while eliminating the need for external ultrasound coupling

medium for photoacoustic imaging. Using this system, they demonstrated photoacoustic microscopy of cortical vascular network in live mice for over 28 days [62].

In addition to polymer materials, silicon microresonators have also been used in acoustic sensing applications, as silicon related technology has been very well developed in semiconductor industry. Silicon on insulator (SOI) wafers can be massively produced, and silicon microresonators are easily scalably fabricated on a chip. In 2020, Shnaiderman et al. demonstrated miniaturized high-sensitivity and ultrabroadband acoustic sensing using an array of point like silicon waveguide-etalon detector using an SOI platform. The cavity is formed by a spacer and a Bragg grating, with a cavity size of only 220 nm by 500 nm, allowing an ultra-small sensing area (Figure 22C). The SOI based optical resonator design provides per-area sensitivity that is 1000 times higher than that of microring resonators and 10^8 times better than that of piezoelectric detectors. This design enables an ultra-wide detection bandwidth, reaching 230 MHz at −6dB [64].

In 2021, Westerveld et al. demonstrated an ultrasound sensor in silicon photonic technology with extreme

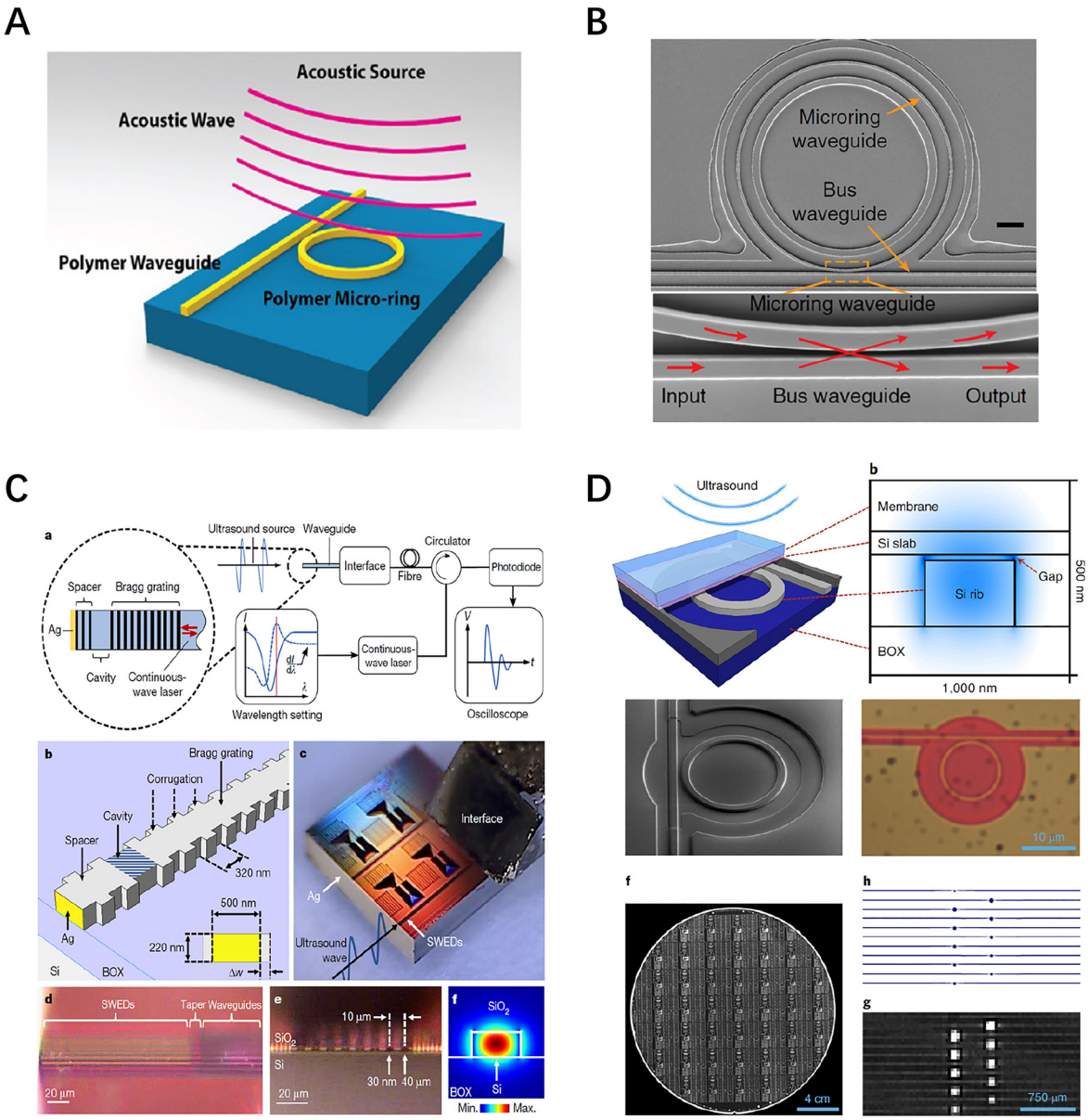

Figure 22: Photoacoustic sensing using integrated resonator systems: (A) polystyrene microring resonator [60]. (B) PDMS microring resonator [62]. (C) Silicon point-like silicon waveguide–etalon detector [64]. (D) Silicon microring resonator coupled with a membrane with a 15 nm air gap in between [65].

sensitivity owing to an innovative optomechanical waveguide. This optomechanical system consists of a silicon microring resonator coupled with a silicon membrane above the microring, with a 15 nm gap in between. The device is fabricated using CMOS-compatible processing, with the schematic of the structure, fabrication flow, SEM images and optical microscope images of the device shown in Figure 22D. The function principle of this optomechanical acoustic sensor is as follows: an external acoustic wave drives the mechanical motion of the membrane, and changes the gap between the membrane and the microring. This induces a change in the effective refractive index of the optical mode and therefore shifts the optical resonance of the microring. As a result, the acoustic signal can be optically readout using this microring resonator. The 20 μm small sensor has a noise equivalent pressure below 1.3 mPa/$\sqrt{\text{Hz}}$ in the measured range of 3–30 MHz, dominated by acoustomechanical noise [65]. This is two orders of magnitude better than for piezoelectric elements of an identical size. Benefitting from the advanced micro/nano fabrication of silicon photonics, this device can be easily massively fabricated on a chip, as shown in the bottom panel of Figure 22D. Photoacoustic imaging is also demonstrated using an array of these devices, coupled with a common waveguide. The demonstrated sensor array with on-chip photonic multiplexing offers the potential of miniaturized catheters with sensor matrices interrogated using just a few optical fibers, unlike piezoelectric sensors that typically use an electrical connection for each element.

4 Quantum enhanced optomechanical sensing

In typical optomechanical sensing devices, coherent light sources are used, which are limited by quantum noises. To reduce the quantum noise below the standard quantum limit and improve the measurement sensitivity, we can use the squeezed light source in place of the coherent light source as the driving light of the optomechanical system. This chapter will introduce the concept of squeezed light and the process of squeezed light improving the measurement sensitivity of the optomechanical system.

4.1 Squeezed light

Consider a single optical mode a, which can be rewritten in a complex-amplitude pattern as

$$a = X_1 + \mathrm{i}X_2. \tag{12}$$

Here, X_1 and X_2 are Hermitian operators representing the two quadrature phases of the mode. Their commutation relation satisfies $\left[X_1, X_2\right] = i/2$. The resulting uncertainty principle is $\Delta X_1 \Delta X_2 \geq 1/4$.

A single-mode coherent light can be described as a coherent state $|\alpha\rangle$. The coherent state is the eigenstate of the annihilation operator a [159], contenting

$$a\,|\alpha\rangle = \alpha\,|\alpha\rangle\,. \tag{13}$$

In the coherent state $|\alpha\rangle$, the expectation values and variances of X_1, X_2 are $\langle X_1 + \mathrm{i}X_2\rangle = \alpha$ and $\Delta X_1 = \Delta X_2 = 1/2$. As Figure 23A shows, in the complex-amplitude plane with X_1 and X_2 axes, a coherent state can be depicted as an "error circle". Here, the center of the circle locates at $X_1 + \mathrm{i}X_2 = \alpha$ representing the expectation value of a coherent state. And the radius $\Delta X_1 = \Delta X_2 = 1/2$ denoting the equal uncertainties of operators X_1 and X_2.

Similarly, the single-mode squeezed light can be denoted as a squeezed state $|\alpha, \zeta\rangle$. Here, $\zeta = r\mathrm{e}^{\mathrm{i}\theta}$ is an arbitrary complex number, where $r = |\zeta|$ is called the squeeze factor [160]. A squeezed state is able to be acquired through first squeezing the vacuum state followed by being acted with the displacement operator $D(\alpha)$:

$$|\alpha, \zeta\rangle = D(\alpha)\, S(\zeta)\, |0\rangle\,, \tag{14}$$

where $S(\zeta) = \exp[\zeta^* a^2/2 - \zeta\left(a^\dagger\right)^2/2]$ is a unitary squeeze operator. Besides, let us define the rotated complex amplitudes:

$$Y_1 + \mathrm{i}Y_2 = (X_1 + \mathrm{i}X_2)\,\mathrm{e}^{-\mathrm{i}\theta/2}\,, \tag{15}$$

in which $\theta/2$ denotes the rotating angle.

In the squeezed state $|\alpha, \zeta\rangle$, expectation values and variances are $\langle X_1 + \mathrm{i}X_2\rangle = \langle Y_1 + \mathrm{i}Y_2\rangle\,\mathrm{e}^{-\mathrm{i}\theta/2} = \alpha$, $\Delta Y_1 = \mathrm{e}^{-r}/2$, $\Delta Y_2 = \mathrm{e}^{r}/2$. The squeezed state has the same expectation values of complex amplitudes as the ones in the corresponding coherent state $|\alpha\rangle$. The uncertainty relation between Y_1 and Y_2: $\Delta Y_1 \Delta Y_2 = 1/4$ still promises the squeezed state is a minimum-uncertainty state. However, the uncertainties of Y_1 and Y_2 are unequal. An "error ellipse" of the squeezed state $|\alpha, \zeta\rangle$ in the complex-amplitude plane is displayed in Figure 23B. Intuitively, the error area of the squeezed state $|\alpha, \zeta\rangle$ is attained by squeezing the one in the coherent state $|\alpha\rangle$ along the Y_1 axi.

In Figure 24, the diagrams of electric field versus time plus the corresponding error area in the complex-amplitude plane with X_1 and X_2 axes are shown for a

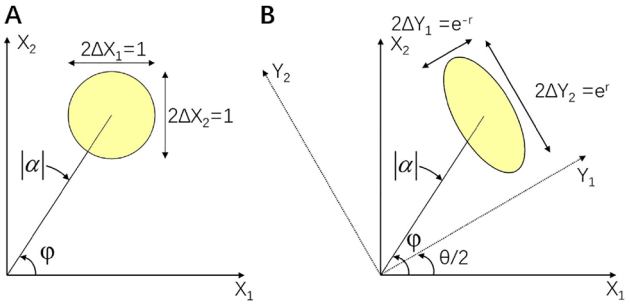

Figure 23: (A) An error circle of coherent state $|\alpha\rangle$ in the complex-amplitude plane. (B) An error ellipse of squeezed state $|\alpha, \zeta\rangle$ in the complex-amplitude plane. The yellow parts of both figures are the error area.

coherent state, a squeezed state reducing the uncertainty in X_1, and a squeezed state reducing the uncertainty in X_2. Each point in the error area, which is colored in yellow, corresponds to a wave with a certain phase and a certain amplitude. The muster of all the waves corresponding to the points in the error area denotes the uncertainties of an electric field, which is colored in purple. Besides, the central black curve in the electric field diagram is the expectation value of the electric field. Compared to a coherent state, a squeezed state reducing the uncertainty in X_1 has less deviation of amplitude while more deviation of phase in electric field. The contrary situation appears in a squeezed state reducing the uncertainty in X_2.

To generate the squeezed light source, the nonlinear process is a key step [161]. Experimentally the main methods are parametric downconversion (PDC) [162] and four-wave mixing (FWM) [163]. The squeezed light source has been realized in various systems such as atomic ensembles [163, 164], nonlinear crystals [162, 165, 166], optical fibers [167–169], microcavity polaritons [170], and cavity optomechanical systems [16–18]. Up to now, the largest degree of quantum noise suppression up to 15 dB has been achieved by H. Vahlbruch et al. utilizing a doubly resonant, non-monolithic optical parametric amplifier cavity in 2016 [166].

Squeezed light can also be obtained in optomechanical systems (Figure 25) since optomechanical coupling is one kind of nonlinear process [171, 172]. In 2012, Brooks generated the squeezed light, whose quantum noise was 1.2% below the shot noise, in an cold-atom optomechanical system [18]. In 2013, Amir et al. realized the light with 4.5% squeezing in a photonic-crystal cavity optomechanical system [16]. In the same year, Purdy et al. employed the membrane-in-the-middle optomechanical system to produce the 32%-squeezing light [17]. Optomechanical systems demonstrate the potential of producing squeezed light.

The squeezed light is capable of enhancing the measurement sensitivity, and has found applications in various fields, such as gravitational wave detection [173, 174], magnetometer [175] and biological measurement [176], which will be discussed in the following section.

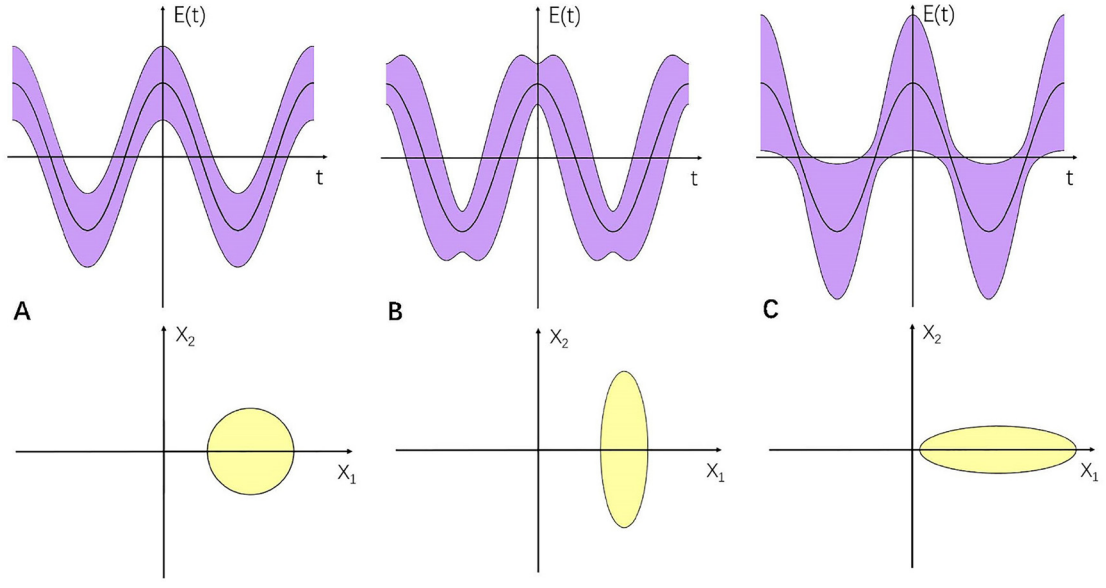

Figure 24: Diagrams of electric field versus time and the corresponding error area in three states. (A) A coherent state. (B) A squeezed state reducing the uncertainty in X_1. (C) A squeezed state reducing the uncertainty in X_2.

4.2 Squeezed light enhanced optomechanical sensing

Squeezed light has been used to suppress the shot noise level, and therefore increase the optomechanical sensitivity [177]. For instance, squeezed light has been used to enhance the sensitivity of the laser interferometer gravitational wave detector. Nearly a century after Einstein first predicted the existence of gravitational waves, a global network of Earth-based gravitational wave observatories (such as LIGO, VERGO, etc.) was seeking to directly detect this extremely weak wave using precision laser interferometry. Photon shot noise, due to the quantum nature of light, imposes a fundamental limit on the attometer-level sensitivity of the kilometer-scale Michelson Interferometers deployed for this task. In 2011, the LIGO Scientific Collaboration demonstrated the first squeezed-light enhancement of GEO 600 [173], and then they performed a long-term application of squeezed vacuum states of light [178]. In particular, squeezed vacuum was applied to GEO 600 during a period of three months from June to August 2011 in the first run, and for another 11 months from November 2011 to October 2012 in the second run. A sensitivity increase from squeezed vacuum application was observed broadband above 400 Hz. The time average of gain in sensitivity was 26% (2.0 dB), determined in the frequency band from 3.7 to 4.0 kHz. This corresponds to a factor of 2 increase in the observed volume of the Universe for sources in the kHz region. Later in 2013, the LIGO Scientific Collaboration injected squeezed states to improve the performance of one of the detectors of the LIGO beyond the quantum noise limit [174], most notably in the frequency region down to 150 Hz, critically important for several astrophysical sources, with no deterioration of performance observed at any frequency. The simplified layout of the interferometer with squeezed vacuum injection is shown in Figure 26A. With the injection of squeezed state, they realized a 2.15 dB sensitivity improvement in the shot noise limited frequency band, as shown in Figure 26B. With this improvement, the LIGO detector demonstrated the best broadband sensitivity to gravitational waves ever achieved.

In addition to the kilometer-scale laser interferometers, squeezed light has also been used in microscale photonic devices and measurements. For instance, it has been used in nanoscale measurement of biological systems [176], and magnetic field measurement using atomic magnetometers [175, 179], In cavity optomechanics, it has been used to enhance displacement measurements [100, 180], improve both feedback [181] and sideband [182] cooling, and study the backaction from the radiation pressure force [183]. For optomechanical sensing applications, squeezed light has been used to enhance the sensitivity and bandwidth of a cavity optomechanical magnetometer [48]. A neodymium-doped yttrium aluminum garnet (Nd:YAG) laser is used to produce squeezed light at a wavelength of 1064 nm. Squeezed light is generated through a parametric down conversion process in a 10 mm periodically polled potassium titanyl phosphate (PPKTP) crystal enclosed in a linear cavity (Figure 26C). Both the 532 nm light (the pump light) and the 1064 nm light (the seed light) are injected into the cavity. To generate phase-squeezed light, the pump phase is locked to the seed beam amplification. The light is coupled into the microtoroid evanescently through an optical nanofiber with a diameter of about 700 nm. The optical resonance of the cavity is thermally tuned to match the wavelength of the laser. A coil is used to produce an AC magnetic field to test the magnetic field response of the magnetometer. The mechanical motion of the toroid is measured by performing homodyne detection. With the use of squeezed light, shot noise in the optomechanical system has been suppressed by about 2.5 dB (Figure 26D). As a result, the magnetic field sensitivity is improved by about 20%, and the 3 dB bandwidth is broadened by about 50%.

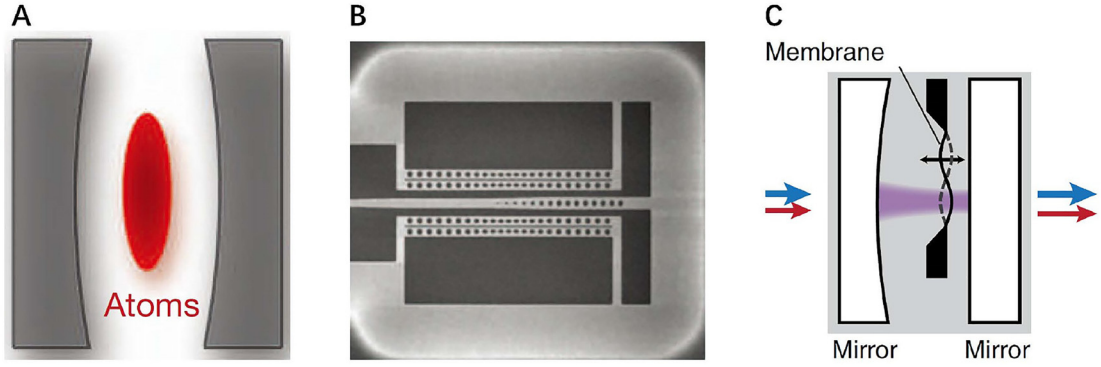

Figure 25: Three types of optomechanical system to realize the squeezed light. (A) Cold-atom optomechanical system [18]. (B) Photonic-crystal cavity optomechanical system [16]. (C) Membrane-in-the-middle optomechanical system [17].

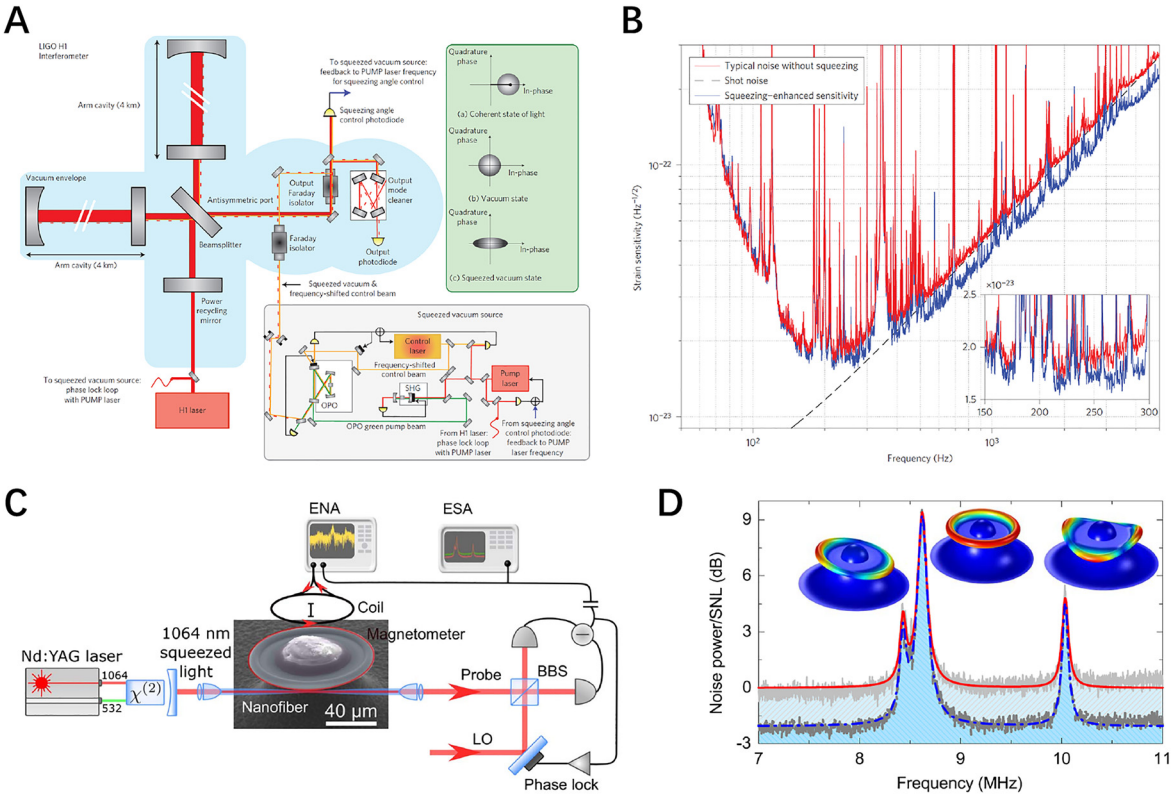

Figure 26: Squeezed light enhanced optomechanical sensing. (A), simplified layout of the interferometer with squeezed vacuum injection. (B) Noise suppression in the shot noise limited frequency band in LIGO with the injection of squeezed light [174]. (C) Measurement setup for the squeeze light enhanced cavity optomechanical magnetometry. (D) Noise power spectra of the cavity optomechanical magnetometry, with coherent probe (red curve) and squeezed probe (blue curve), showing a 2.5 dB noise suppression in the shot noise limited frequency band [48].

5 Summary and outlook

Cavity optomechanical systems provide an ideal platform for precision sensing. In this paper, we review the recent research progress in precision optomechanical sensing, including the sensing principle, sensing platforms, various sensing applications, and squeezed light enhanced sensing. We have provided examples of optomechanical sensors for displacement sensing, mass sensing, force sensing, atomic force microscopy and magnetic resonance force microscopy, acceleration sensing, magnetic field sensing, and acoustic sensing. In recent years, these examples have moved beyond proof-of-principle and towards real applications. With the development of modern micro/nano fabrication technology, more and more chip-scale sensing platforms have been developed and used for versatile sensing applications. Further improvements are needed for better performance of cavity optomechanical sensors, to meet the requirements for specific applications. For instance, for cavity optomechanical magnetometers, their sensitivities at low frequency ranges (from DC to 100 Hz) still need to be improved, for applications such as magnetic anomaly detection and MEG. For cavity optomechanical acoustic sensors, their sensitivities at high frequency ranges (from MHz to GHz) are to be further improved for applications such as medical imaging and photoacoustic sensing. In addition, in order to achieve more robust, portable, and cheaper devices, integration of the lasers and photodetectors with the on-chip optomechanical sensors are required in the future. With their superior sensitivity, broad bandwidth, low power consumption, on-chip integration capability, and high technology readiness, moving forward, we believe these precision optomechanical sensors will find applications in real world in the near future.

Author contribution: All the authors contributed to the writing and revision of the manuscript.

Research funding: The National Natural Science Foundation of China (NSFC) (E0J2021L21, 11934019, 61705259, 92050110, 91736106, 1674390, and 91836302), the basic frontier science research program of Chinese Academy of Sciences (ZDBS-LY- JSC003), the Key-Area Research and

Development Program of Guangdong Province (Grant No. 2019B030330001), and the National Key R&D Program of China (Grants No. 2018YFA0306504).

Conflict of interest statement: The authors declare no conflicts of interest regarding this article.

References

[1] M. Aspelmeyer, T. J. Kippenberg, and F. Marquardt, "Cavity optomechanics," *Rev. Mod. Phys.*, vol. 86, no. 4, p. 1391, 2014.

[2] W. P. Bowen and G. J. Milburn, *Quantum Optomechanics*, CRC Press, Boca Raton, 2016.

[3] M. Aspelmeyer, T. J. Kippenberg, and F. Marquardt, *Cavity Optomechanics*, Springer, New York, 2014.

[4] T. J. Kippenberg and K. J. Vahala, "Cavity opto-mechanics," *Opt. Express*, vol. 15, no. 25, pp. 17172–17205, 2007.

[5] T. J. Kippenberg and K. J. Vahala, "Cavity optomechanics: back-action at the mesoscale," *Science*, vol. 321, no. 5893, pp. 1172–1176, 2008.

[6] P. Meystre, "A short walk through quantum optomechanics," *Ann. Phys.*, vol. 525, no. 3, pp. 215–233, 2013.

[7] A. Schliesser, R. Rivière, G. Anetsberger, O. Arcizet, and T. J. Kippenberg, "Resolved-sideband cooling of a micromechanical oscillator," *Nat. Phys.*, vol. 4, no. 5, pp. 415–419, 2008.

[8] A. Schliesser, O. Arcizet, R. Rivière, G. Anetsberger, and T. J. Kippenberg, "Resolved-sideband cooling and position measurement of a micromechanical oscillator close to the Heisenberg uncertainty limit," *Nat. Phys.*, vol. 5, no. 7, pp. 509–514, 2009.

[9] A. D. O'Connell, M. Hofheinz, M. Ansmann, et al., "Quantum ground state and single-phonon control of a mechanical resonator," *Nature*, vol. 464, no. 7289, pp. 697–703, 2010.

[10] J. Chan, T. P. Alegre, A. H. Safavi-Naeini, et al., "Laser cooling of a nanomechanical oscillator into its quantum ground state," *Nature*, vol. 478, no. 7367, pp. 89–92, 2011.

[11] J. D. Teufel, T. Donner, D. Li, et al., "Sideband cooling of micromechanical motion to the quantum ground state," *Nature*, vol. 475, no. 7356, pp. 359–363, 2011.

[12] A. Szorkovszky, A. C. Doherty, G. I. Harris, and W. P. Bowen, "Mechanical squeezing via parametric amplification and weak measurement," *Phys. Rev. Lett.*, vol. 107, no. 21, p. 213603, 2011.

[13] E. E. Wollman, C. U. Lei, A. J. Weinstein, et al., "Quantum squeezing of motion in a mechanical resonator," *Science*, vol. 349, no. 6251, p. 952, 2015.

[14] F. Lecocq, J. B. Clark, R. W. Simmonds, J. Aumentado, and J. D. Teufel, "Quantum nondemolition measurement of a nonclassical state of a massive object," *Phys. Rev. X*, vol. 5, no. 4, 2015, Art no. 041037.

[15] J. M. Pirkkalainen, E. Damskägg, M. Brandt, F. Massel, and M. A. Sillanpää, "Squeezing of quantum noise of motion in a micromechanical resonator," *Phys. Rev. Lett.*, vol. 115, no. 24, p. 243601, 2015.

[16] A. H. Safavi-Naeini, S. Gröblacher, J. T. Hill, J. Chan, M. Aspelmeyer, and O. Painter, "Squeezed light from a silicon micromechanical resonator," *Nature*, vol. 500, no. 7461, pp. 185–189, 2013.

[17] T. P. Purdy, P.-L. Yu, R. Peterson, N. Kampel, and C. Regal, "Strong optomechanical squeezing of light," *Phys. Rev. X*, vol. 3, no. 3, 2013, Art no. 031012.

[18] D. W. Brooks, T. Botter, S. Schreppler, T. P. Purdy, N. Brahms, and D. M. Stamper-Kurn, "Non-classical light generated by quantum-noise-driven cavity optomechanics," *Nature*, vol. 488, no. 7412, pp. 476–480, 2012.

[19] S. Weis, R. Rivière, S. Deléglise, et al., "Optomechanically induced transparency," *Science*, vol. 330, no. 6010, pp. 1520–1523, 2010.

[20] C. Dong, V. Fiore, M. C. Kuzyk, and H. Wang, "Optomechanical dark mode," *Science*, vol. 338, no. 6114, pp. 1609–1613, 2012.

[21] S. Gröblacher, K. Hammerer, M. R. Vanner, and M. Aspelmeyer, "Observation of strong coupling between a micromechanical resonator and an optical cavity field," *Nature*, vol. 460, no. 7256, pp. 724–727, 2009.

[22] R. Riedinger, S. Hong, R. A. Norte, et al., "Non-classical correlations between single photons and phonons from a mechanical oscillator," *Nature*, vol. 530, no. 7590, pp. 313–316, 2016.

[23] H. Xu, D. Mason, L. Jiang, and J. Harris, "Topological energy transfer in an optomechanical system with exceptional points," *Nature*, vol. 537, no. 7618, pp. 80–83, 2016.

[24] H. Xu, L. Jiang, A. A. Clerk, and J. G. E. Harris, "Nonreciprocal control and cooling of phonon modes in an optomechanical system," *Nature*, vol. 568, no. 7750, pp. 65–69, 2019.

[25] Z. Shen, Y.-L. Zhang, Y. Chen, et al., "Experimental realization of optomechanically induced non-reciprocity," *Nat. Photonics*, vol. 10, no. 10, pp. 657–661, 2016.

[26] K. Fang, J. Luo, A. Metelmann, et al., "Generalized non-reciprocity in an optomechanical circuit via synthetic magnetism and reservoir engineering," *Nat. Phys.*, vol. 13, no. 5, pp. 465–471, 2017.

[27] N. R. Bernier, L. D. Toth, A. Koottandavida, et al., "Nonreciprocal reconfigurable microwave optomechanical circuit," *Nat. Commun.*, vol. 8, no. 1, pp. 1–8, 2017.

[28] L. M. de Lépinay, C. F. Ockeloen-Korppi, D. Malz, and M. A. Sillanpää, "Nonreciprocal transport based on cavity floquet modes in optomechanics," *Phys. Rev. Lett.*, vol. 125, no. 2, 2020, Art no. 023603.

[29] R. Riedinger, A. Wallucks, I. Marinković, et al., "Remote quantum entanglement between two micromechanical oscillators," *Nature*, vol. 556, no. 7702, pp. 473–477, 2018.

[30] S. Kiesewetter, R. Teh, P. Drummond, and M. Reid, "Pulsed entanglement of two optomechanical oscillators and Furry's hypothesis," *Phys. Rev. Lett.*, vol. 119, no. 2, 2017, Art no. 023601.

[31] A. Schliesser, G. Anetsberger, R. Rivière, O. Arcizet, and T. J. Kippenberg, "High-sensitivity monitoring of micromechanical vibration using optical whispering gallery mode resonators," *New J. Phys.*, vol. 10, no. 9, 2008, Art no. 095015.

[32] Y.-W. Hu, Y.-F. Xiao, Y.-C. Liu, and Q. Gong, "Optomechanical sensing with on-chip microcavities," *Front. Phys.*, vol. 8, no. 5, pp. 475–490, 2013.

[33] M. Metcalfe, "Applications of cavity optomechanics," *Appl. Phys. Rev.*, vol. 1, no. 3, p. 031105, 2014.

[34] M. Sansa, M. Defoort, A. Brenac, et al., "Optomechanical mass spectrometry," *Nat. Commun.*, vol. 11, no. 1, p. 3781, 2020.
[35] E. Gavartin, P. Verlot, and T. J. Kippenberg, "A hybrid on-chip optomechanical transducer for ultrasensitive force measurements," *Nat. Nanotechnol.*, vol. 7, no. 8, pp. 509–514, 2012.
[36] K. Srinivasan, H. Miao, M. T. Rakher, M. Davanco, and V. Aksyuk, "Optomechanical transduction of an integrated silicon cantilever probe using a microdisk resonator," *Nano Lett.*, vol. 11, no. 2, pp. 791–797, 2011.
[37] J. Chae, S. An, G. Ramer, et al., "Nanophotonic atomic force microscope transducers enable chemical composition and thermal conductivity measurements at the nanoscale," *Nano Lett.*, vol. 17, no. 9, pp. 5587–5594, 2017.
[38] P. E. Allain, L. Schwab, C. Mismer, et al., "Optomechanical resonating probe for very high frequency sensing of atomic forces," *Nanoscale*, vol. 12, no. 5, pp. 2939–2945, 2020.
[39] H. J. Mamin, R. Budakian, B. W. Chui, and D. Rugar, "Detection and manipulation of statistical polarization in small spin ensembles," *Phys. Rev. Lett.*, vol. 91, no. 20, p. 207604, 2003.
[40] D. Rugar, R. Budakian, H. J. Mamin, and B. W. Chui, "Single spin detection by magnetic resonance force microscopy," *Nature*, vol. 430, no. 6997, pp. 329–332, 2004.
[41] R. Fischer, D. P. McNally, C. Reetz, et al., "Spin detection with a micromechanical trampoline: towards magnetic resonance microscopy harnessing cavity optomechanics," *New J. Phys.*, vol. 21, no. 4, p. 043049, 2019.
[42] A. G. Krause, M. Winger, T. D. Blasius, Q. Lin, and O. Painter, "A high-resolution microchip optomechanical accelerometer," *Nat. Photonics*, vol. 6, no. 11, p. 768, 2012.
[43] F. G. Cervantes, L. Kumanchik, J. Pratt, and J. M. Taylor, "High sensitivity optomechanical reference accelerometer over 10 kHz," *Appl. Phys. Lett.*, vol. 104, no. 22, p. 221111, 2014.
[44] S. Forstner, S. Prams, J. Knittel, et al., "Cavity optomechanical magnetometer," *Phys. Rev. Lett.*, vol. 108, no. 12, p. 120801, 2012.
[45] S. Forstner, E. Sheridan, J. Knittel, et al., "Ultrasensitive optomechanical magnetometry," *Adv. Mater.*, vol. 26, no. 36, pp. 6348–6353, 2014.
[46] C. Yu, J. Janousek, E. Sheridan, et al., "Optomechanical magnetometry with a macroscopic resonator," *Phys. Rev. Appl.*, vol. 5, no. 4, p. 044007, 2016.
[47] B.-B. Li, D. Bulla, V. Prakash, et al., "Invited article: scalable high-sensitivity optomechanical magnetometers on a chip," *APL Photonics*, vol. 3, no. 12, p. 120806, 2018.
[48] B.-B. Li, J. Bílek, U. B. Hoff, et al., "Quantum enhanced optomechanical magnetometry," *Optica*, vol. 5, no. 7, pp. 850–856, 2018.
[49] B.-B. Li, G. Brawley, H. Greenall, et al., "Ultrabroadband and sensitive cavity optomechanical magnetometry," *Photon. Res.*, vol. 8, no. 7, pp. 1064–1071, 2020.
[50] J. Zhu, G. Zhao, I. Savukov, and L. Yang, "Polymer encapsulated microcavity optomechanical magnetometer," *Sci. Rep.*, vol. 7, no. 1, p. 8896, 2017.
[51] E. Freeman, C. Y. Wang, V. Sumaria, S. J. Schiff, Z. Liu, and S. Tadigadapa, "Chip-scale high q-factor glassblown microspherical shells for magnetic sensing," *AIP Adv.*, vol. 8, no. 6, 2018, Art no. 065214.
[52] M. F. Colombano, G. Arregui, F. Bonell, et al., "Ferromagnetic resonance assisted optomechanical magnetometer," *Phys. Rev. Lett.*, vol. 125, no. 14, p. 147201, 2020.
[53] M. Wu, N. L. Wu, T. Firdous, et al., "Nanocavity optomechanical torque magnetometry and radiofrequency susceptometry," *Nat. Nanotechnol.*, vol. 12, no. 2, pp. 127–131, 2017.
[54] F. Monifi, B. Peng, K. Özdemir, et al., "Ultrasound sensing using a fiber coupled silica microtoroid resonator encapsulated in a polymer," in *2013 IEEE Photonics Conference*, 2013, pp. 215–216.
[55] M. V. Chistiakova and A. M. Armani, "Photoelastic ultrasound detection using ultra-high-q silica optical resonators," *Opt. Express*, vol. 22, no. 23, pp. 28169–28179, 2014.
[56] K. H. Kim, W. Luo, C. Zhang, et al., "Air-coupled ultrasound detection using capillary-based optical ring resonators," *Sci. Rep.*, vol. 7, no. 1, p. 109, 2017.
[57] S. Basiri-Esfahani, A. Armin, S. Forstner, and W. P. Bowen, "Precision ultrasound sensing on a chip," *Nat. Commun.*, vol. 10, no. 1, p. 132, 2019.
[58] J. Pan, B. Zhang, Z. Liu, et al., "Microbubble resonators combined with a digital optical frequency comb for high-precision air-coupled ultrasound detectors," *Photon. Res.*, vol. 8, no. 3, pp. 303–310, 2020.
[59] J. A. Guggenheim, J. Li, T. J. Allen, et al., "Ultrasensitive plano-concave optical microresonators for ultrasound sensing," *Nat. Photonics*, vol. 11, no. 11, pp. 714–719, 2017.
[60] C. Zhang, T. Ling, S.-L. Chen, and L. J. Guo, "Ultrabroad bandwidth and highly sensitive optical ultrasonic detector for photoacoustic imaging," *ACS Photonics*, vol. 1, no. 11, pp. 1093–1098, 2014.
[61] H. Li, B. Dong, Z. Zhang, H. F. Zhang, and C. Sun, "A transparent broadband ultrasonic detector based on an optical micro-ring resonator for photoacoustic microscopy," *Sci. Rep.*, vol. 4, p. 4496, 2014.
[62] H. Li, B. Dong, X. Zhang, et al., "Disposable ultrasound-sensing chronic cranial window by soft nanoimprinting lithography," *Nat. Commun.*, vol. 10, no. 1, p. 4277, 2019.
[63] J. Yang, T. Qin, F. Zhang, X. Chen, X. Jiang, and W. Wan, "Multiphysical sensing of light, sound and microwave in a microcavity Brillouin laser," *Nanophotonics*, vol. 9, no. 9, pp. 2915–2925, 2020.
[64] R. Shnaiderman, G. Wissmeyer, O. Ulgen, Q. Mustafa, A. Chmyrov, and V. Ntziachristos, "A submicrometre silicon-on-insulator resonator for ultrasound detection," *Nature*, vol. 585, no. 7825, pp. 372–378, 2020.
[65] W. J. Westerveld, M. Mahmud-Ul-Hasan, R. Shnaiderman, et al., "Sensitive, small, broadband and scalable optomechanical ultrasound sensor in silicon photonics," *Nat. Photonics*, vol. 15, no. 5, pp. 341–345, 2021.
[66] C. Law, "Interaction between a moving mirror and radiation pressure: a Hamiltonian formulation," *Phys. Rev. A*, vol. 51, no. 3, p. 2537, 1995.
[67] W. Yu, W. C. Jiang, Q. Lin, and T. Lu, "Cavity optomechanical spring sensing of single molecules," *Nat. Commun.*, vol. 7, p. 12311, 2016.

[68] E. Gil-Santos, J. J. Ruz, O. Malvar, et al., "Optomechanical detection of vibration modes of a single bacterium," *Nat. Nanotechnol.*, vol. 15, no. 6, pp. 469–474, 2020.
[69] E. Verhagen, S. Deléglise, S. Weis, A. Schliesser, and T. J. Kippenberg, "Quantum-coherent coupling of a mechanical oscillator to an optical cavity mode," *Nature*, vol. 482, no. 7383, pp. 63–67, 2012.
[70] G. S. Wiederhecker, L. Chen, A. Gondarenko, and M. Lipson, "Controlling photonic structures using optical forces," *Nature*, vol. 462, no. 7273, pp. 633–636, 2009.
[71] P. H. Kim, B. D. Hauer, C. Doolin, F. Souris, and J. P. Davis, "Approaching the standard quantum limit of mechanical torque sensing," *Nat. Commun.*, vol. 7, p. 13165, 2016.
[72] G. S. MacCabe, H. Ren, J. Luo, et al., "Nano-acoustic resonator with ultralong phonon lifetime," *Science*, vol. 370, no. 6518, pp. 840–843, 2020.
[73] M. Eichenfield, R. Camacho, J. Chan, K. J. Vahala, and O. Painter, "A picogram-and nanometre-scale photonic-crystal optomechanical cavity," *Nature*, vol. 459, no. 7246, pp. 550–555, 2009.
[74] M. Wu, A. C. Hryciw, C. Healey, et al., "Dissipative and dispersive optomechanics in a nanocavity torque sensor," *Phys. Rev. X*, vol. 4, no. 2, p. 021052, 2014.
[75] K. J. Vahala, "Optical microcavities," *Nature*, vol. 424, no. 6950, pp. 839–846, 2003.
[76] D. K. Armani, T. J. Kippenberg, S. M. Spillane, and K. J. Vahala, "Ultra-high-q toroid microcavity on a chip," *Nature*, vol. 421, no. 6926, pp. 925–928, 2003.
[77] G. Anetsberger, R. Rivière, A. Schliesser, O. Arcizet, and T. J. Kippenberg, "Ultralow-dissipation optomechanical resonators on a chip," *Nat. Photonics*, vol. 2, no. 10, pp. 627–633, 2008.
[78] C. G. Baker, C. Bekker, D. L. McAuslan, E. Sheridan, and W. P. Bowen, "High bandwidth on-chip capacitive tuning of microtoroid resonators," *Opt. Express*, vol. 24, no. 18, pp. 20400–20412, 2016.
[79] X. Jiang, Q. Lin, J. Rosenberg, K. Vahala, and O. Painter, "High-q double-disk microcavities for cavity optomechanics," *Opt. Express*, vol. 17, no. 23, pp. 20911–20919, 2009.
[80] Q. Lin, J. Rosenberg, X. Jiang, K. J. Vahala, and O. Painter, "Mechanical oscillation and cooling actuated by the optical gradient force," *Phys. Rev. Lett.*, vol. 103, no. 10, p. 103601, 2009.
[81] J. Rosenberg, Q. Lin, and O. Painter, "Static and dynamic wavelength routing via the gradient optical force," *Nat. Photonics*, vol. 3, no. 8, pp. 478–483, 2009.
[82] G. S. Wiederhecker, S. Manipatruni, S. Lee, and M. Lipson, "Broadband tuning of optomechanical cavities," *Opt. Express*, vol. 19, no. 3, pp. 2782–2790, 2011.
[83] C. Bekker, C. G. Baker, R. Kalra, et al., "Free spectral range electrical tuning of a high quality on-chip microcavity," *Opt. Express*, vol. 26, no. 26, pp. 33649–33670, 2018.
[84] G. Anetsberger, O. Arcizet, Q. P. Unterreithmeier, et al., "Near-field cavity optomechanics with nanomechanical oscillators," *Nat. Phys.*, vol. 5, no. 12, pp. 909–914, 2009.
[85] P. H. Kim, B. D. Hauer, T. J. Clark, F. Fani Sani, M. R. Freeman, and J. P. Davis, "Magnetic actuation and feedback cooling of a cavity optomechanical torque sensor," *Nat. Commun.*, vol. 8, no. 1, p. 1355, 2017.
[86] G. I. Harris, D. L. McAuslan, E. Sheridan, Y. Sachkou, C. Baker, and W. P. Bowen, "Laser cooling and control of excitations in superfluid helium," *Nat. Phys.*, vol. 12, no. 8, pp. 788–793, 2016.
[87] L. Childress, M. P. Schmidt, A. D. Kashkanova, et al., "Cavity optomechanics in a levitated helium drop," *Phys. Rev.*, vol. 96, no. 6, 2017, Art no. 063842.
[88] M. Eichenfield, J. Chan, R. M. Camacho, K. J. Vahala, and O. Painter, "Optomechanical crystals," *Nature*, vol. 462, no. 7269, pp. 78–82, 2009.
[89] F. Pan, K. Cui, G. Bai, et al., "Radiation-pressure-antidamping enhanced optomechanical spring sensing," *ACS Photonics*, vol. 5, no. 10, pp. 4164–4169, 2018.
[90] L. Ding, C. Baker, P. Senellart, et al., "High frequency GaAs nano-optomechanical disk resonator," *Phys. Rev. Lett.*, vol. 105, no. 26, p. 263903, 2010.
[91] G. Anetsberger, E. Gavartin, O. Arcizet, et al., "Measuring nanomechanical motion with an imprecision below the standard quantum limit," *Phys. Rev. A*, vol. 82, no. 6, 2010, Art no. 061804.
[92] D. J. Wilson, V. Sudhir, N. Piro, R. Schilling, A. Ghadimi, and T. J. Kippenberg, "Measurement-based control of a mechanical oscillator at its thermal decoherence rate," *Nature*, vol. 524, no. 7565, pp. 325–329, 2015.
[93] H. Zhang, X. Zhao, Y. Wang, Q. Huang, and J. Xia, "Femtogram scale high frequency nano-optomechanical resonators in water," *Opt. Express*, vol. 25, no. 2, pp. 821–830, 2017.
[94] J. D. Teufel, T. Donner, M. Castellanos-Beltran, J. W. Harlow, and K. W. Lehnert, "Nanomechanical motion measured with an imprecision below that at the standard quantum limit," *Nat. Nanotechnol.*, vol. 4, no. 12, pp. 820–823, 2009.
[95] Ž. Zobenica, R. W. van der Heijden, M. Petruzzella, et al., "Integrated nano-opto-electro-mechanical sensor for spectrometry and nanometrology," *Nat. Commun.*, vol. 8, no. 1, pp. 1–8, 2017.
[96] F. Galeotti, I. S. Vollenbroek, M. Petruzzella, et al., "On-chip waveguide-coupled opto-electro-mechanical system for nanoscale displacement sensing," *APL Photonics*, vol. 5, no. 2, 2020, Art no. 026103.
[97] O. Arcizet, P.-F. Cohadon, T. Briant, et al., "High-sensitivity optical monitoring of a micromechanical resonator with a quantum-limited optomechanical sensor," *Phys. Rev. Lett.*, vol. 97, no. 13, p. 133601, 2006.
[98] S. Tallur and S. A. Bhave, "Rayleigh scattering boosted multi-gHz displacement sensitivity in whispering gallery opto-mechanical resonators," *Opt. Express*, vol. 21, no. 23, pp. 27780–27788, 2013.
[99] T. Liu, F. Pagliano, R. van Veldhoven, V. Pogoretskiy, Y. Jiao, and A. Fiore, "Integrated nano-optomechanical displacement sensor with ultrawide optical bandwidth," *Nat. Commun.*, vol. 11, no. 1, pp. 1–7, 2020.
[100] U. B. Hoff, G. I. Harris, L. S. Madsen, et al., "Quantum-enhanced micromechanical displacement sensitivity," *Opt. Lett.*, vol. 38, no. 9, pp. 1413–1415, 2013.
[101] V. Peano, H. Schwefel, C. Marquardt, and F. Marquardt, "Intracavity squeezing can enhance quantum-limited optomechanical position detection through deamplification," *Phys. Rev. Lett.*, vol. 115, no. 24, p. 243603, 2015.

[102] N. Kampel, R. Peterson, R. Fischer, et al., "Improving broadband displacement detection with quantum correlations," *Phys. Rev. X*, vol. 7, no. 2, 2017, Art no. 021008.
[103] D. Mason, J. Chen, M. Rossi, Y. Tsaturyan, and A. Schliesser, "Continuous force and displacement measurement below the standard quantum limit," *Nat. Phys.*, vol. 15, no. 8, pp. 745–749, 2019.
[104] U. S. Sainadh and M. A. Kumar, "Displacement sensing beyond the standard quantum limit with intensity-dependent optomechanical coupling," *Phys. Rev.*, vol. 102, no. 6, 2020, Art no. 063523.
[105] J. Griffiths, "A brief history of mass spectrometry," *Anal. Chem.*, vol. 80, no. 15, pp. 5678–5683, 2008.
[106] J.-J. Li and K.-D. Zhu, "All-optical mass sensing with coupled mechanical resonator systems," *Phys. Rep.*, vol. 525, no. 3, pp. 223–254, 2013.
[107] J. Chaste, A. Eichler, J. Moser, G. Ceballos, R. Rurali, and A. Bachtold, "A nanomechanical mass sensor with yoctogram resolution," *Nat. Nanotechnol.*, vol. 7, no. 5, pp. 301–304, 2012.
[108] A. K. Naik, M. Hanay, W. Hiebert, X. Feng, and M. L. Roukes, "Towards single-molecule nanomechanical mass spectrometry," *Nat. Nanotechnol.*, vol. 4, no. 7, pp. 445–450, 2009.
[109] F. Liu, S. Alaie, Z. C. Leseman, and M. Hossein-Zadeh, "Sub-pg mass sensing and measurement with an optomechanical oscillator," *Opt. Express*, vol. 21, no. 17, pp. 19555–19567, 2013.
[110] W. Yu, W. C. Jiang, Q. Lin, and T. Lu, "Cavity optomechanical spring sensing of single molecules," *Nat. Commun.*, vol. 7, no. 1, pp. 1–9, 2016.
[111] S. a. Dohn, W. Svendsen, A. Boisen, and O. Hansen, "Mass and position determination of attached particles on cantilever based mass sensors," *Rev. Sci. Instrum.*, vol. 78, no. 10, p. 103303, 2007.
[112] S. Dohn, R. Sandberg, W. Svendsen, and A. Boisen, "Enhanced functionality of cantilever based mass sensors using higher modes," *Appl. Phys. Lett.*, vol. 86, no. 23, p. 233501, 2005.
[113] J.-J. Li and K.-D. Zhu, "Nonlinear optical mass sensor with an optomechanical microresonator," *Appl. Phys. Lett.*, vol. 101, no. 14, p. 141905, 2012.
[114] C. Jiang, Y. Cui, and K.-D. Zhu, "Ultrasensitive nanomechanical mass sensor using hybrid opto-electromechanical systems," *Opt. Express*, vol. 22, no. 11, pp. 13773–13783, 2014.
[115] Y. He, "Sensitivity of optical mass sensor enhanced by optomechanical coupling," *Appl. Phys. Lett.*, vol. 106, no. 12, p. 121905, 2015.
[116] Q. Lin, B. He, and M. Xiao, "Mass sensing by detecting the quadrature of a coupled light field," *Phys. Rev. A*, vol. 96, no. 4, 2017, Art no. 043812.
[117] J. Liu and K.-D. Zhu, "Room temperature optical mass sensor with an artificial molecular structure based on surface plasmon optomechanics," *Photon. Res.*, vol. 6, no. 9, pp. 867–874, 2018.
[118] S. Liu, B. Liu, J. Wang, T. Sun, and W.-X. Yang, "Realization of a highly sensitive mass sensor in a quadratically coupled optomechanical system," *Phys. Rev. A*, vol. 99, no. 3, 2019, Art no. 033822.
[119] H. Miao, K. Srinivasan, and V. Aksyuk, "A microelectromechanically controlled cavity optomechanical sensing system," *New J. Phys.*, vol. 14, no. 7, 2012, Art no. 075015.
[120] G. I. Harris, D. L. McAuslan, T. M. Stace, A. C. Doherty, and W. P. Bowen, "Minimum requirements for feedback enhanced force sensing," *Phys. Rev. Lett.*, vol. 111, no. 10, p. 103603, 2013.
[121] A. Vinante, M. Bonaldi, F. Marin, and J. Zendri, "Dissipative feedback does not improve the optimal resolution of incoherent force detection," *Nat. Nanotechnol.*, vol. 8, no. 7, p. 470, 2013.
[122] E. Gavartin, P. Verlot, and T. Kippenberg, "Reply to 'dissipative feedback does not improve the optimal resolution of incoherent force detection'," *Nat. Nanotechnol.*, vol. 8, no. 10, p. 692, 2013.
[123] S. Schreppler, N. Spethmann, N. Brahms, T. Botter, M. Barrios, and D. M. Stamper-Kurn, "Optically measuring force near the standard quantum limit," *Science*, vol. 344, no. 6191, pp. 1486–1489, 2014.
[124] P. Weber, J. Güttinger, A. Noury, J. Vergara-Cruz, and A. Bachtold, "Force sensitivity of multilayer graphene optomechanical devices," *Nat. Commun.*, vol. 7, no. 1, pp. 1–8, 2016.
[125] C. Doolin, P. Kim, B. Hauer, A. MacDonald, and J. Davis, "Multidimensional optomechanical cantilevers for high-frequency force sensing," *New J. Phys.*, vol. 16, no. 3, 2014, Art no. 035001.
[126] C. Regal, J. Teufel, and K. Lehnert, "Measuring nanomechanical motion with a microwave cavity interferometer," *Nat. Phys.*, vol. 4, no. 7, pp. 555–560, 2008.
[127] A. Motazedifard, F. Bemani, M. Naderi, R. Roknizadeh, and D. Vitali, "Force sensing based on coherent quantum noise cancellation in a hybrid optomechanical cavity with squeezed-vacuum injection," *New J. Phys.*, vol. 18, no. 7, 2016, Art no. 073040.
[128] X. Xu and J. M. Taylor, "Squeezing in a coupled two-mode optomechanical system for force sensing below the standard quantum limit," *Phys. Rev. A*, vol. 90, no. 4, 2014, Art no. 043848.
[129] L. Buchmann, S. Schreppler, J. Kohler, N. Spethmann, and D. Stamper-Kurn, "Complex squeezing and force measurement beyond the standard quantum limit," *Phys. Rev. Lett.*, vol. 117, no. 3, 2016, Art no. 030801.
[130] S. Huang and G. Agarwal, "Robust force sensing for a free particle in a dissipative optomechanical system with a parametric amplifier," *Phys. Rev. A*, vol. 95, no. 2, 2017, Art no. 023844.
[131] A. Motazedifard, A. Dalafi, F. Bemani, and M. Naderi, "Force sensing in hybrid Bose–Einstein-condensate optomechanics based on parametric amplification," *Phys. Rev. A*, vol. 100, no. 2, 2019, Art no. 023815.
[132] T. Caniard, P. Verlot, T. Briant, P.-F. Cohadon, and A. Heidmann, "Observation of back-action noise cancellation in interferometric and weak force measurements," *Phys. Rev. Lett.*, vol. 99, no. 11, p. 110801, 2007.
[133] T. Gebremariam, Y.-X. Zeng, M. Mazaheri, and C. Li, "Enhancing optomechanical force sensing via precooling and

quantum noise cancellation,'' *Sci. China Phys. Mech. Astron.*, vol. 63, no. 1, pp. 1–11, 2020.
[134] A. Mehmood, S. Qamar, and S. Qamar, ''Effects of laser phase fluctuation on force sensing for a free particle in a dissipative optomechanical system,'' *Phys. Rev.*, vol. 98, no. 5, 2018, Art no. 053841.
[135] Y. Liu, H. Miao, V. Aksyuk, and K. Srinivasan, ''Wide cantilever stiffness range cavity optomechanical sensors for atomic force microscopy,'' *Opt. Express*, vol. 20, no. 16, pp. 18268–18280, 2012.
[136] A. Sheinker, L. Frumkis, B. Ginzburg, N. Salomonski, and B. Kaplan, ''Magnetic anomaly detection using a three-axis magnetometer,'' *IEEE Trans. Magn.*, vol. 45, no. 1, pp. 160–167, 2009.
[137] A. Edelstein, ''Advances in magnetometry,'' *J. Phys. Condens. Matter*, vol. 19, no. 16, p. 165217, 2007.
[138] D. R. Glenn, D. B. Bucher, J. Lee, M. D. Lukin, H. Park, and R. L. Walsworth, ''High-resolution magnetic resonance spectroscopy using a solid-state spin sensor,'' *Nature*, vol. 555, no. 7696, pp. 351–354, 2018.
[139] I. Savukov and T. Karaulanov, ''Magnetic-resonance imaging of the human brain with an atomic magnetometer,'' *Appl. Phys. Lett.*, vol. 103, no. 4, 2013, Art no. 043703.
[140] H. Xia, A. Ben-Amar Baranga, D. Hoffman, and M. V. Romalis, ''Magnetoencephalography with an atomic magnetometer,'' *Appl. Phys. Lett.*, vol. 89, no. 21, p. 211104, 2006.
[141] E. Boto, N. Holmes, J. Leggett, et al., ''Moving magnetoencephalography towards real-world applications with a wearable system,'' *Nature*, vol. 555, no. 7698, pp. 657–661, 2018.
[142] J. R. Kirtley, M. B. Ketchen, K. G. Stawiasz, et al., ''High-resolution scanning squid microscope,'' *Appl. Phys. Lett.*, vol. 66, no. 9, pp. 1138–1140, 1995.
[143] J. R. Kirtley, L. Paulius, A. J. Rosenberg, et al., ''Scanning squid susceptometers with sub-micron spatial resolution,'' *Rev. Sci. Instrum.*, vol. 87, no. 9, 2016, Art no. 093702.
[144] H. B. Dang, A. C. Maloof, and M. V. Romalis, ''Ultrahigh sensitivity magnetic field and magnetization measurements with an atomic magnetometer,'' *Appl. Phys. Lett.*, vol. 97, no. 15, p. 151110, 2010.
[145] M. Vengalattore, J. M. Higbie, S. R. Leslie, J. Guzman, L. E. Sadler, and D. M. Stamper-Kurn, ''High-resolution magnetometry with a spinor Bose–Einstein condensate,'' *Phys. Rev. Lett.*, vol. 98, no. 20, p. 200801, 2007.
[146] J. M. Taylor, P. Cappellaro, L. Childress, et al., ''High-sensitivity diamond magnetometer with nanoscale resolution,'' *Nat. Phys.*, vol. 4, no. 10, pp. 810–816, 2008.
[147] T. Wolf, P. Neumann, K. Nakamura, et al., ''Subpicotesla diamond magnetometry,'' *Phys. Rev. X*, vol. 5, no. 4, 2015, Art no. 041001.
[148] F. Xu, S. Guo, Y. Yu, et al., ''Method for assembling nanosamples and a cantilever for dynamic cantilever magnetometry,'' *Phys. Rev. Appl.*, vol. 11, no. 5, p. 054007, 2019.
[149] Y. Yu, F. Xu, S. Guo, et al., ''Inferring the magnetic anisotropy of a nanosample through dynamic cantilever magnetometry measurements,'' *Appl. Phys. Lett.*, vol. 116, no. 19, p. 193102, 2020.
[150] J. P. Davis, D. Vick, D. C. Fortin, J. A. J. Burgess, W. K. Hiebert, and M. R. Freeman, ''Nanotorsional resonator torque magnetometry,'' *Appl. Phys. Lett.*, vol. 96, no. 7, p. 072513, 2010.
[151] J. P. Davis, D. Vick, P. Li, et al., ''Nanomechanical torsional resonator torque magnetometry (invited),'' *J. Appl. Phys.*, vol. 109, no. 7, p. 07D309, 2011.
[152] J. P. Davis, D. Vick, J. A. J. Burgess, et al., ''Observation of magnetic supercooling of the transition to the vortex state,'' *New J. Phys.*, vol. 12, no. 9, p. 093033, 2010.
[153] J. A. J. Burgess, A. E. Fraser, F. F. Sani, et al., ''Quantitative magneto–mechanical detection and control of the barkhausen effect,'' *Science*, vol. 339, no. 6123, p. 1051, 2013.
[154] J. E. Losby, Z. Diao, F. Fani Sani, et al., ''Nanomechanical ac susceptometry of an individual mesoscopic ferrimagnet,'' *Solid State Commun.*, vol. 198, pp. 3–6, 2014.
[155] J. E. Losby, F. F. Sani, D. T. Grandmont, et al., ''Torque-mixing magnetic resonance spectroscopy,'' *Science*, vol. 350, no. 6262, p. 798, 2015.
[156] J. Losby, J. A. J. Burgess, Z. Diao, D. C. Fortin, W. K. Hiebert, and M. R. Freeman, ''Thermo-mechanical sensitivity calibration of nanotorsional magnetometers,'' *J. Appl. Phys.*, vol. 111, no. 7, p. 07D305, 2012.
[157] P. H. Kim, C. Doolin, B. D. Hauer, et al., ''Nanoscale torsional optomechanics,'' *Appl. Phys. Lett.*, vol. 102, no. 5, p. 053102, 2013.
[158] P. H. Kim, F. Fani Sani, M. R. Freeman, and J. P. Davis, ''Broadband optomechanical transduction of nanomagnetic spin modes,'' *Appl. Phys. Lett.*, vol. 113, no. 8, 2018, Art no. 083104.
[159] R. J. Glauber, ''Coherent and incoherent states of the radiation field,'' *Phys. Rev.*, vol. 131, no. 6, p. 2766, 1963.
[160] C. M. Caves, ''Quantum-mechanical noise in an interferometer,'' *Phys. Rev. D*, vol. 23, no. 8, p. 1693, 1981.
[161] C. Xu, L. Zhang, S. Huang, et al., ''Sensing and tracking enhanced by quantum squeezing,'' *Photon. Res.*, vol. 7, no. 6, pp. A14–A26, 2019.
[162] L.-A. Wu, H. Kimble, J. Hall, and H. Wu, ''Generation of squeezed states by parametric down conversion,'' *Phys. Rev. Lett.*, vol. 57, no. 20, p. 2520, 1986.
[163] R. Slusher, L. Hollberg, B. Yurke, J. Mertz, and J. Valley, ''Observation of squeezed states generated by four-wave mixing in an optical cavity,'' *Phys. Rev. Lett.*, vol. 55, no. 22, p. 2409, 1985.
[164] A. M. Guerrero, P. Nussenzveig, M. Martinelli, A. Marino, and H. Florez, ''Quantum noise correlations of an optical parametric oscillator based on a nondegenerate four wave mixing process in hot alkali atoms,'' *Phys. Rev. Lett.*, vol. 125, no. 8, 2020, Art no. 083601.
[165] H. Vahlbruch, M. Mehmet, S. Chelkowski, et al., ''Observation of squeezed light with 10-dB quantum-noise reduction,'' *Phys. Rev. Lett.*, vol. 100, no. 3, 2008, Art no. 033602.
[166] H. Vahlbruch, M. Mehmet, K. Danzmann, and R. Schnabel, ''Detection of 15 dB squeezed states of light and their application for the absolute calibration of photoelectric quantum efficiency,'' *Phys. Rev. Lett.*, vol. 117, no. 11, p. 110801, 2016.

[167] R. Shelby, M. Levenson, S. Perlmutter, R. DeVoe, and D. Walls, "Broad-band parametric deamplification of quantum noise in an optical fiber," *Phys. Rev. Lett.*, vol. 57, no. 6, p. 691, 1986.
[168] M. Rosenbluh and R. Shelby, "Squeezed optical solitons," *Phys. Rev. Lett.*, vol. 66, no. 2, p. 153, 1991.
[169] S. Schmitt, J. Ficker, M. Wolff, F. König, A. Sizmann, and G. Leuchs, "Photon-number squeezed solitons from an asymmetric fiber-optic sagnac interferometer," *Phys. Rev. Lett.*, vol. 81, no. 12, p. 2446, 1998.
[170] T. Boulier, M. Bamba, A. Amo, et al., "Polariton-generated intensity squeezing in semiconductor micropillars," *Nat. Commun.*, vol. 5, no. 1, pp. 1–7, 2014.
[171] C. Fabre, M. Pinard, S. Bourzeix, A. Heidmann, E. Giacobino, and S. Reynaud, "Quantum-noise reduction using a cavity with a movable mirror," *Phys. Rev. A*, vol. 49, no. 2, p. 1337, 1994.
[172] S. Mancini and P. Tombesi, "Quantum noise reduction by radiation pressure," *Phys. Rev. A*, vol. 49, no. 5, p. 4055, 1994.
[173] J. Abadie, B. P. Abbott, R. Abbott, et al., "A gravitational wave observatory operating beyond the quantum shot-noise limit," *Nat. Phys.*, vol. 7, no. 12, p. 962, 2011.
[174] J. Aasi, J. Abadie, B. Abbott, et al., "Enhanced sensitivity of the ligo gravitational wave detector by using squeezed states of light," *Nat. Photonics*, vol. 7, no. 8, pp. 613–619, 2013.
[175] F. Wolfgramm, A. Cere, F. A. Beduini, A. Predojević, M. Koschorreck, and M. W. Mitchell, "Squeezed-light optical magnetometry," *Phys. Rev. Lett.*, vol. 105, no. 5, 2010, Art no. 053601.
[176] M. A. Taylor, J. Janousek, V. Daria, et al., "Biological measurement beyond the quantum limit," *Nat. Photonics*, vol. 7, no. 3, pp. 229–233, 2013.
[177] B. J. Lawrie, P. D. Lett, A. M. Marino, and R. C. Pooser, "Quantum sensing with squeezed light," *ACS Photonics*, vol. 6, no. 6, pp. 1307–1318, 2019.
[178] H. Grote, K. Danzmann, K. L. Dooley, R. Schnabel, J. Slutsky, and H. Vahlbruch, "First long-term application of squeezed states of light in a gravitational-wave observatory," *Phys. Rev. Lett.*, vol. 110, no. 18, p. 181101, 2013.
[179] T. Horrom, R. Singh, J. P. Dowling, and E. E. Mikhailov, "Quantum-enhanced magnetometer with low-frequency squeezing," *Phys. Rev. A*, vol. 86, no. 2, p. 023803, 2012.
[180] R. C. Pooser and B. Lawrie, "Ultrasensitive measurement of microcantilever displacement below the shot-noise limit," *Optica*, vol. 2, no. 5, pp. 393–399, 2015.
[181] C. Schafermeier, H. Kerdoncuff, U. B. Hoff, et al., "Quantum enhanced feedback cooling of a mechanical oscillator using nonclassical light," *Nat. Commun.*, vol. 7, p. 13628, 2016.
[182] J. B. Clark, F. Lecocq, R. W. Simmonds, J. Aumentado, and J. D. Teufel, "Sideband cooling beyond the quantum backaction limit with squeezed light," *Nature*, vol. 541, no. 7636, pp. 191–195, 2017.
[183] J. B. Clark, F. Lecocq, R. W. Simmonds, J. Aumentado, and J. D. Teufel, "Observation of strong radiation pressure forces from squeezed light on a mechanical oscillator," *Nat. Phys.*, vol. 12, no. 7, pp. 683–687, 2016.